



Dynamic Inversion based Full Envelope Flight Control for an eVTOL Vehicle using a Unified Framework

Thomas Lombaerts* John Kaneshige† Stefan Schuet‡ Gordon Hardy§
Bimal Aponso¶ Kimberlee Shish||
NASA Ames Research Center, Moffett Field, CA 94035

Urban Air Mobility is a future mode of transportation that will require a revolutionary new vehicle concept. One of the concepts currently being studied and developed are eVTOL (electrical vertical takeoff and landing) vehicles. This paper discusses a nonlinear dynamic inversion based control law that was designed for this vehicle concept. Two advantageous inherent properties of dynamic inversion in this setup are the effective decoupling of the control axes which are by design highly coupled for this kind of vehicle, and its ability to naturally handle changes of operating condition, which removes the need for gain scheduling. These are advantageous for control of VTOL vehicles, due to their wide range of operating conditions which varies from hover to forward flight, and transitioning between them. The inner dynamic inversion control loop, including an optimization based blended control allocation strategy to the rotors as well as to the control surfaces, serves as an inner core flight control system for the full envelope. This setup is complemented with a set of linear controllers, and reference models as well as command filtering for the different manual control modes in the various flight phases. An autoflight mode is included as well. By using Incremental Nonlinear Dynamic Inversion, it was found that the overall controller becomes significantly less dependent on accurate aircraft model properties, especially with respect to the aerodynamic derivatives, of which one can expect limited knowledge for this kind of UAM vehicles.

Nomenclature

α	angle of attack [rad]	G	nonlinear function matrix which maps inputs
β	sideslip angle [rad]	I	inertia matrix [slugs ft ²]
$\delta_{a/e/r}$	aileron/elevator/rudder deflection [deg]	M	moment vector [lbs ft ² /s ²]
δ_{fl}	flaps setting [deg]	p	parameter vector
δ_{T_i}	tilt angle of propeller i [rad]	u	input vector
$\delta_{T_{c_i}}$	throttle setting [0–1]	V	speed [kts]
η	blending coefficient [0–1]	W	weighting matrix
γ	flight path angle [rad]	x	state vector
ω	angular rate vector [rad/s]	τ_{eng}	engine time constant [s]
ν	virtual input	b	wingspan [ft]
ω_n	natural frequency [rad/s]	C_D	drag coefficient [-]
$\phi/\theta/\psi$	roll / pitch attitude / yaw angle [rad]	C_L	lift coefficient [-]
ρ	air density [slugs/ft ³]	C_p	pressure coefficient [-]
ζ	damping coefficient [0–1]	C_\bullet	dimensionless force or moment coefficient [-]
\bar{c}	mean aerodynamic chord [ft]	c_{T_i}	thrust coefficient of the rotor
\bar{q}	$= \frac{1}{2}\rho V^2$, dynamic pressure [slugs/(ft s ²)]	D_i	rotor diameter [ft]
\mathcal{M}_{CA}	control efficiencies matrix	$dx_f/dy_f/dz_f$	location front propeller wrt cg [ft]
F	force vector [lbs ft/s ²]	$dx_r/dy_r/dz_r$	location rear propeller wrt cg [ft]
f	nonlinear state function vector	F	force [lbs ft/s ²]
		g	gravity constant [ft/s ²]

*Aerospace Research Engineer, Stinger Ghaffarian Technologies, Intelligent Systems Division, Mail Stop 269-1, AIAA Associate Fellow, thomas.lombaerts@nasa.gov

†Computer Engineer, Intelligent Systems Division, Mail Stop 269-1, AIAA member.

‡Computer Engineer, Intelligent Systems Division, Mail Stop 269-3, AIAA member.

§Research Pilot, Science Applications International Corporation, Moffett Field, California 94035, AIAA member.

¶Chief, Aeronautics Projects Office, Mail Stop 210-14, AIAA Associate Fellow

||Aerospace Engineer, Intelligent Systems Division, Mail Stop 269-1, AIAA member.

h	altitude [ft]	$X/Y/Z$	force vector components [lbs ft/s ²]
I_{\bullet}	scalar for mass inertia [slugs ft ²]	0	with respect to trim or previous condition
k_m	torque constant of the propellers	aero	aerodynamics
K_{\bullet}	controller gain	BW	bandwidth
$L/M/N$	moment vector components [lbs ft ² /s ²]	comm	commanded
m	mass [lbs]	fil	filter
n_{prop}	number of rotors	grav	gravity
$p/q/r$	roll / pitch / yaw rate [rad/s]	prop	propeller
RPM	rotations per minute	ref	reference
S	wing surface area [ft ²]	req	required
T_i	thrust provided by propeller i [lbs]	vert	vertical

I. Introduction

RECENTLY, there have been numerous developments in the area of urban air taxi operations, also known as urban air mobility or on-demand mobility applications that help to meet the challenging mobility needs of an increasing population density, taking into account the limited capacity of the currently available transportation infrastructure. One of the enabling technologies of this transportation concept is the vertical take-off and landing (VTOL) capability, where power and energy requirements are minimized by using low disk-loading rotors, and short range requirements permit consideration of non-traditional propulsion concepts. This is helped by the latest advances in the technological fields of structures, automation and control, scaling of propulsion systems, and energy-storage. The combination of these technologies and capabilities promises to lead to the opportunity to design unconventional new means of transportation, such as urban air mobility with electrical VTOL capability[1, 2].

Currently, a diverse range of vehicle configurations are being explored, designed and flight tested, such as the Munich based company Lilium with their two-seat Eagle and five-seat Jet, the Silicon Valley based Airbus subsidiary A³ with the Vahana, the Volocopter VC2 near Stuttgart, Santa Cruz based Joby Aviation with the S2 and Lotus, and Mountain View based Wisk (previously Kitty Hawk) with the Cora, among many others. Although currently not in the design-build-fly phase, two independent sets of common reference models (CRM) are noteworthy, one provided by NASA[3, 4] and the other by Uber Elevate. These are virtual designs which can be used by industry and academia as engineering models for technology development. These vehicles are roughly divided into three sub-groups, based on their propulsion configuration:

- 1) tilting propulsion system: Lilium Eagle and Jet, A³ Vahana, Joby Aviation S2 and Lotus, NASA tiltwing CRM.
- 2) separate vertical and forward propulsion system: Wisk Cora, Aurora PAV, NASA lift+cruise CRM.
- 3) vertical propulsion system only: Volocopter VC2, NASA quadrotor CRM.

Another grouping is based on ‘winged eVTOL’ versus ‘wingless eVTOL’ designs, among many other possibilities.

An important advantage of tilting propulsion systems is the flexibility to carry heavier payloads. In case of heavy loading and adverse atmospheric conditions (so-called ‘hot and high’ conditions with lower air density) which prevent a vertical takeoff, the propulsion system can tilt to a certain optimal angle, which would allow for a short takeoff roll.

A. Focus of this paper

This paper builds further on the work of Ref. [5] and investigates the automation and control challenges of the wide range of flying conditions over the full flight envelope, varying from hover to forward flight and the transitions between them. The inner dynamic inversion control loop, including an optimization based blended control allocation strategy to the rotors as well as to the control surfaces, serves as an inner core flight control system for the full envelope, which is a similar strategy as the approach taken in Ref. [6]. The expected lack of detailed model information of these vehicles is an additional robustness challenge tackled by the control system, by relying on a novel control technique that needs less detailed vehicle model information. Building further on the work in Ref. [5], this paper considers some of the handling qualities requirements for the approach and landing phase.

B. Literature survey

Most control system design literature focuses on the control of quadcopters and other vertical propulsion configurations. Among others, Model Reference Adaptive Control (MRAC) is a popular approach for these applications, in order to deal with large parameter uncertainties[7]. Other popular approaches are eigenstructure assignment[8] and

Nonlinear Dynamic Inversion (NDI)[9]. The incremental approach, called incremental nonlinear dynamic inversion (INDI) is beneficial in this kind of application, because this method requires little modeling and is computationally efficient[10, 11]. However, since this approach relies on the so-called time scale separation principle, it is not mathematically rigorous. There is also a lack of stability and robustness analysis for INDI. Therefore, Ref. [12] reformulated the INDI control law without using the time scale separation principle. The stability of the closed-loop system in the presence of external disturbances was analyzed using Lyapunov methods and nonlinear system perturbation theory. Also, the robustness of the closed-loop system against regular and singular perturbations was analyzed. Another familiar constraint of NDI is actuator saturation. Ref. [13] used Incremental Nonlinear Control Allocation to solve this problem for a tailless aircraft with highly coupled control effectors.

Nonlinear Dynamic Inversion is the chosen control approach for the research presented in this paper. This method facilitates the physical interpretation of internal signals. Other important advantages are:

- 1) Perfect decoupling of the steering channels, which results in a significantly simplified steering task.
- 2) The control laws are split into a model dependent part and a model independent part. In this way, gain scheduling is not needed.
- 3) The total control structure involves reference models for command shaping. This is an adequate setup for complying with flying and handling qualities and for incorporating signals that hedge against control saturation as well as envelope protection.

This control setup applied on the class of vehicles studied here, however, is especially prone to control saturation. Therefore, specific protections are needed, such as prioritized control allocation and pseudo control hedging, among others.

C. Paper Structure

The structure of this paper is as follows. The simulation model is described in Sec. II. Sec. III gives a brief recap and comparison of the concepts of nonlinear dynamic inversion (NDI) and incremental NDI (INDI). Then Sec. IV implements the NDI and INDI control laws for this specific class of vehicle. This includes prioritized control allocation to avoid control saturation in Sec. IV.B.2. This section ends with the discussion of the linear controllers and the reference models and command filtering for the different flight phases, such as translational rate command (TRC) for the landing phase. Initial simulation results are presented in Sec. V. These results focus primarily on demonstrating the full envelope flying capabilities of the control setup. Sec. V.C analyses how this control setup complies with the TRC requirements in the ADS-33 Flying and Handling Qualities requirements. Finally, Sec. VI presents the conclusions and recommendations.

II. Simulation Model

A conceptual UAM eVTOL configuration, similar to a Cessna TTx, was used for this concept study. This vehicle has separate lift and cruise rotors, as shown in Fig. 1. A few key characteristics of the vehicle are given in Table 1. The flight mechanics and the propulsion system of the vehicle are described in the remainder of this section.



Fig. 1 Illustration of the conceptual vehicle

property	value
mass m	2650 lbs
mass inertia I_{xx}	948 slugs ft ²
mass inertia I_{yy}	1346 slugs ft ²
mass inertia I_{zz}	1967 slugs ft ²
mass inertia I_{xz}	0 slugs ft ² (Ref. [14])
wing area S	174 ft ²
wingspan b	36 ft
length l	25.16 ft
capacity	1 pilot + 3 pax
number of lift rotors	4
number of cruise rotors	1

Table 1 Technical specifications of the vehicle

A. Flight Mechanics

The universal kinematic equations for linear and angular accelerations are:

$$\dot{\mathbf{V}} = \frac{1}{m} (\mathbf{F}_{\text{total}} - \boldsymbol{\omega} \times m \mathbf{V}) \quad (1)$$

$$\dot{\boldsymbol{\omega}} = \mathbf{I}^{-1} (\mathbf{M}_{\text{total}} - \boldsymbol{\omega} \times \mathbf{I} \boldsymbol{\omega}) \quad (2)$$

where the total force and moment vectors consist of contributions from aerodynamics, propulsion and gravity:

$$\mathbf{F}_{\text{total}} = \mathbf{F}_{\text{aero}} + \mathbf{F}_{\text{prop}} + \mathbf{F}_{\text{grav}} \quad (3)$$

$$\mathbf{M}_{\text{total}} = \mathbf{M}_{\text{aero}} + \mathbf{M}_{\text{prop}} \quad (4)$$

The aerodynamic contributions are defined by means of their dimensionless coefficients as follows:

$$\mathbf{F}_{\text{aero}} = \begin{bmatrix} X_{\text{aero}} \\ Y_{\text{aero}} \\ Z_{\text{aero}} \end{bmatrix} = \begin{bmatrix} C_X \\ C_Y \\ C_Z \end{bmatrix} \bar{q} S \quad (5)$$

$$\mathbf{M}_{\text{aero}} = \begin{bmatrix} L_{\text{aero}} \\ M_{\text{aero}} \\ N_{\text{aero}} \end{bmatrix} = \begin{bmatrix} b C_l \\ \bar{c} C_m \\ b C_n \end{bmatrix} \bar{q} S \quad (6)$$

where the dimensionless aerodynamic force coefficients are a blending of the conventional lift, drag and sideforce coefficients and the corresponding flat plate coefficients, which is transformed from the aerodynamic reference frame to the body reference frame:

$$\begin{bmatrix} C_X \\ C_Y \\ C_Z \end{bmatrix} = \begin{bmatrix} \cos \alpha & 0 & -\sin \alpha \\ 0 & 1 & 0 \\ \sin \alpha & 0 & \cos \alpha \end{bmatrix} \begin{bmatrix} \cos \beta & -\sin \beta & 0 \\ \sin \beta & \cos \beta & 0 \\ 0 & 0 & 1 \end{bmatrix} \begin{bmatrix} -C_D \\ -C_Y \\ -C_L \end{bmatrix} \quad (7)$$

$$\begin{bmatrix} C_D \\ C_Y \\ C_L \end{bmatrix} = (1 - \eta_{\text{aero} \rightarrow \text{hover}}) \begin{bmatrix} C_D \\ C_Y \\ C_L \end{bmatrix}_{\text{aero}} + \eta_{\text{aero} \rightarrow \text{hover}} \begin{bmatrix} C_D \\ C_Y \\ C_L \end{bmatrix}_{\text{flat plate}} \quad (8)$$

$$\begin{bmatrix} C_D \\ C_Y \\ C_L \end{bmatrix}_{\text{flat plate}} = \begin{bmatrix} C_p \sin \alpha \cos \beta \\ C_p \sin \beta \\ C_p \sin \alpha \cos \alpha \end{bmatrix} \quad (9)$$

$\eta_{\text{aero} \rightarrow \text{hover}}$ is the blending coefficient between hover and forward flight and varies gradually between 0 and 1 and vice versa during transition phases. This coefficient depends on the airspeed. In full hover $\eta_{\text{aero} \rightarrow \text{hover}}$ is 1 and in pure forward flight it is 0. Eq. (9) is based on conventional aerodynamic modeling of a flat plate, with $C_p = 2$. [15, 16] In a similar way, the blending is applied to the aerodynamic moments, where no flat plate effects are expected on the dimensionless aerodynamic moment coefficients:

$$\begin{bmatrix} C_l \\ C_m \\ C_n \end{bmatrix} = (1 - \eta_{\text{aero} \rightarrow \text{hover}}) \begin{bmatrix} C_l \\ C_m \\ C_n \end{bmatrix}_{\text{aero}} \quad (10)$$

The dimensionless aerodynamic moment coefficients depend both on the relevant aerodynamic states as well as the aerodynamic control effectors (control surfaces), as follows:

$$\begin{bmatrix} C_l \\ C_m \\ C_n \end{bmatrix}_{\text{aero}} = \begin{bmatrix} C_l(\beta, p, r) \\ C_m(\alpha, q, \delta_{\text{fl}}) \\ C_n(\beta, p, r) \end{bmatrix} + \begin{bmatrix} C_{l_{\delta_a}} & 0 & C_{l_{\delta_r}} \\ 0 & C_{m_{\delta_e}} & 0 \\ C_{n_{\delta_a}} & 0 & C_{n_{\delta_r}} \end{bmatrix} \cdot \begin{bmatrix} \delta_a \\ \delta_e \\ \delta_r \end{bmatrix} \quad (11)$$

where:

$$\begin{bmatrix} C_l(\beta, p, r) \\ C_m(\alpha, q, \delta_{\text{fl}}) \\ C_n(\beta, p, r) \end{bmatrix} = \begin{bmatrix} C_{l_0} + C_{l_\beta}\beta + C_{l_p}\frac{pb}{2V_{\text{TAS}}} + C_{l_r}\frac{rb}{2V_{\text{TAS}}} \\ C_{m_0}(\delta_{\text{fl}}) + C_{m_\alpha}\alpha + C_{m_q}\frac{qc}{V_{\text{TAS}}} \\ C_{n_0} + C_{n_\beta}\beta + C_{n_p}\frac{pb}{2V_{\text{TAS}}} + C_{n_r}\frac{rb}{2V_{\text{TAS}}} \end{bmatrix} \quad (12)$$

The gravity contribution is:

$$\mathbf{F}_{\text{grav}} = \begin{bmatrix} X_{\text{grav}} \\ Y_{\text{grav}} \\ Z_{\text{grav}} \end{bmatrix} = \begin{bmatrix} -\sin\theta \\ \sin\phi \cos\theta \\ \cos\phi \cos\theta \end{bmatrix} mg \quad (13)$$

The propulsion contributions depend largely on thrust magnitude as well as the tilt angle of the individual nacelles, and the moment arms as defined in Fig. 2:

$$\mathbf{F}_{\text{prop}} = \begin{bmatrix} X_{\text{prop}} \\ Y_{\text{prop}} \\ Z_{\text{prop}} \end{bmatrix} = \begin{bmatrix} \sum_{i=1}^{N_{\text{prop}}} T_i \cos\delta_{T_i} \\ 0 \\ -\sum_{i=1}^{N_{\text{prop}}} T_i \sin\delta_{T_i} \end{bmatrix} \quad (14)$$

$$\mathbf{M}_{\text{prop}} = \begin{bmatrix} L_{\text{prop}} \\ M_{\text{prop}} \\ N_{\text{prop}} \end{bmatrix} = \mathcal{M}_{\text{CA}_{\text{prop}}} \begin{bmatrix} T_1 \\ T_2 \\ T_3 \\ T_4 \end{bmatrix} \quad (15)$$

with:

$$\mathcal{M}_{\text{CA}_{\text{prop}}} = \begin{bmatrix} dy_f \sin\delta_{T_1} - k_m \cos\delta_{T_1} & -dy_f \sin\delta_{T_2} + k_m \cos\delta_{T_2} & dy_r \sin\delta_{T_3} + k_m \cos\delta_{T_3} & -dy_r \sin\delta_{T_4} - k_m \cos\delta_{T_4} \\ dx_f \sin\delta_{T_1} + dz_f \cos\delta_{T_1} & dx_f \sin\delta_{T_2} + dz_f \cos\delta_{T_2} & -dx_r \sin\delta_{T_3} - dz_r \cos\delta_{T_3} & -dx_r \sin\delta_{T_4} - dz_r \cos\delta_{T_4} \\ k_m \sin\delta_{T_1} + dy_f \cos\delta_{T_1} & -k_m \sin\delta_{T_2} - dy_f \cos\delta_{T_2} & -k_m \sin\delta_{T_3} + dy_r \cos\delta_{T_3} & k_m \sin\delta_{T_4} - dy_r \cos\delta_{T_4} \end{bmatrix} \quad (16)$$

In Eq. (16), k_m is the torque constant of the propellers.

B. Propulsion system for thrust modeling

The conceptual propulsion system of this vehicle consists of electric motors, and is represented by a simplified model, based on Ref. [17]. A few key performance characteristics are given in Table 2. Aerodynamic effects between the rotors and their interaction with the fuselage and wings are currently not modeled. Future work will include more detailed propulsion systems.

Table 2 Some key performance characteristics per rotor

characteristic	vertical	cruise
diameter D	2.5 ft	6.5 ft
tilt angle δ_T	90 deg	0 deg
max thrust T_{max}	1325 lbs	760 lbs
thrust coefficient c_T	0.9	
engine time constant τ_{eng}	1/3 s	

Since this vehicle is based on RPM control, the throttle setting is translated into a commanded RPM setting, which is limited corresponding to the minimum and maximum thrust values. Subsequently the commanded RPM setting is used for calculating the commanded thrust levels, and the engine dynamics are represented by a first order engine time constant.

The commanded RPM value per rotor depends on the throttle setting $\delta_{T_{c_i}}$ which is restricted to the range $[0 - 1]$, within some predefined bounds:

$$RPM_{i_{\text{comm}}} = \sqrt{\delta_{T_{c_i}}} (RPM_{\text{max}_i} - RPM_{\text{min}_i}) + RPM_{\text{min}_i} \quad (17)$$

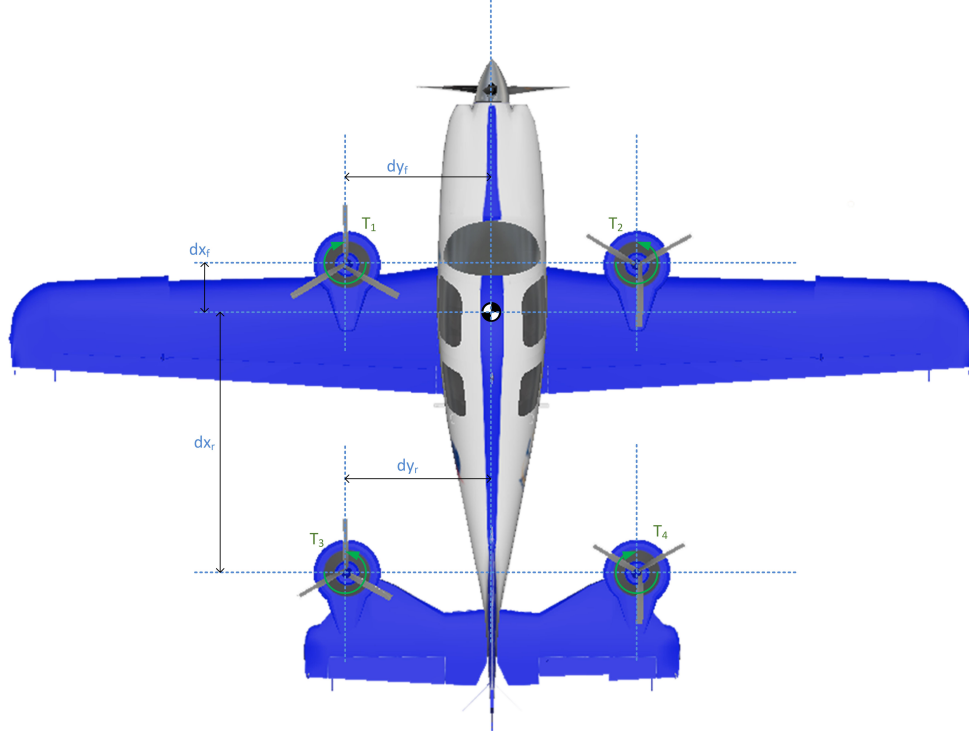


Fig. 2 Geometry of the UAM concept model

Subscript i represents the index of the rotor: $i = 1, 2, \dots, n_{\text{prop}}$ with n_{prop} the total number of rotors. These bounds are based on the maximum and minimum thrust values:

$$RPM_{i_{\max}} = \sqrt{\frac{T_{i_{\max}}}{c_{T_i} \rho D_i^6}} \times 60 \quad (18)$$

$$RPM_{i_{\min}} = \sqrt{\frac{T_{i_{\min}}}{c_{T_i} \rho D_i^6}} \times 60 \quad (19)$$

The actual commanded thrust per rotor is then calculated based on the commanded RPM :

$$T_{i_{\text{comm}}} = c_{T_i} \left(\frac{RPM_{i_{\text{comm}}}}{60} \right)^2 \rho D_i^6 \quad (20)$$

The engine dynamics are represented as follows:

$$\dot{T}_i = -\frac{1}{\tau_{\text{eng}}} (T_i - T_{i_{\text{comm}}}) \quad (21)$$

For electric RPM propulsion, the time delay becomes significantly larger as compared to the more conventional blade pitch control approach, resulting in a time constant $\tau_{\text{eng}} = 1/3s^{-1}$. Earlier research has shown that such a significant time delay will cause difficulties for satisfying the level 1 ADS-33 Handling and Flying Qualities requirements in hover and low speed for small and moderate amplitude attitude changes.[5]

III. Essentials of Nonlinear Dynamic Inversion

A more extensive general discussion and derivation of the regular and incremental nonlinear dynamic inversion control laws, by means of Lie derivatives, is given in Ref. [5]. This section will recapitulate the most important concepts, in order to highlight the essentials and the differences between both.

A. The concept of nonlinear dynamic inversion

The general idea of nonlinear dynamic inversion is as follows. Consider the nonlinear first order MIMO system dynamic model, which is assumed to be affine in the input:

$$\dot{\mathbf{x}} = \mathbf{f}(\mathbf{x}, \mathbf{p}) + \mathbf{G}(\mathbf{x}, \mathbf{p})\mathbf{u} \quad (22)$$

Solving for \mathbf{u} by introducing a virtual outer loop control input vector \mathbf{v} :

$$\mathbf{u} = \mathbf{G}^{-1}(\hat{\mathbf{x}}, \hat{\mathbf{p}}) [\mathbf{v} - \mathbf{f}(\hat{\mathbf{x}}, \hat{\mathbf{p}})] \quad (23)$$

By making use of Nonlinear Dynamic Inversion (NDI), the nonlinear aircraft dynamics can be canceled out such that the resulting system behaves like a pure single r^{th} order integrator. In eq. (23), $\mathbf{f}(\hat{\mathbf{x}}, \hat{\mathbf{p}})$ represents the airframe/engine model and $\mathbf{G}(\hat{\mathbf{x}}, \hat{\mathbf{p}})$ is the so-called effector blending model. Note that the effector blending model $\mathbf{G}(\hat{\mathbf{x}}, \hat{\mathbf{p}})$ needs to be inverted. More information is available in the literature[18, 19].

It should be noted that this dynamic inversion is not perfect due to the presence of the multiplicative uncertainties in the aerodynamic model. However, in past applications the linear controller has shown to be capable to deal with these modeling errors.[20, 21]

B. The concept of incremental nonlinear dynamic inversion

The incremental form of NDI is based on the computation of the control increment at a given point in time with respect to the condition of the system one incremental time instant in the past.[10, 22–26] Recently, this concept received a lot of attention from the flight control community and was test flown by DLR as early as 2013.

The following control law is obtained:

$$\Delta \mathbf{u} \simeq \mathbf{G}(\hat{\mathbf{x}}_0, \hat{\mathbf{p}})^{-1} [\mathbf{v} - \dot{\hat{\mathbf{x}}}_0] \quad (24)$$

Note that it is assumed that \mathbf{G} is invertible. The vector $\dot{\hat{\mathbf{x}}}_0$ contains the state derivatives of inputs computed or estimated from \mathbf{y} or \mathbf{y}_0 , respectively. In the ideal case ($\hat{\mathbf{x}}_0 = \mathbf{x}_0$, $\dot{\hat{\mathbf{x}}}_0 = \dot{\mathbf{x}}_0$, $\hat{\mathbf{p}} = \mathbf{p}$), the input-output response is approximately equal to an integrator. The total input can be obtained by adding the calculated increment to the current input \mathbf{u}_0 :

$$\mathbf{u} = \mathbf{u}_0 + \Delta \mathbf{u} \quad (25)$$

The fundamental difference with conventional NDI is that only partial knowledge of the system dynamics is required as the resulting control law only depends on the control effectiveness $\mathbf{G}(\mathbf{x}, \mathbf{p})$ and not on the airframe/engine model $\mathbf{f}(\hat{\mathbf{x}}, \hat{\mathbf{p}})$. INDI is subsequently less sensitive to model mismatches (i.e. $\hat{\mathbf{p}} \neq \mathbf{p}$), being only dependent on a subset of the uncertain model parameters in \mathbf{p} . However, additional feedback signals are required in the form of state derivatives and the input. In addition, the controller should be discretized with a sufficiently high sampling rate. Finally it should be noted that synchronization between the input and state derivative is required as the calculated control increment is based on a linearisation around a specific operating condition in time.

IV. Overview of nonlinear controller

The overall controller structure consists of four major modules, namely pilot command filtering for rate commands, reference model, and the actual controller which contains the dynamic inversion block as well as a linear controller, as illustrated in Fig. 3. This general setup is very similar to the setup that was used for a previous flight control project for a conventional aircraft configuration[20].

More detail about which quantities are controlled per stage is shown in Fig. 4. The pilot command filtering merely transforms the commands, as provided by the pilot through the control inceptors or the autoflight commands in case of autoflight mode, to commanded values of attitude angles, altitude and airspeed. These are then fed into the second order reference model. By choosing proper values for natural frequency and damping ratio in the reference model, the flying qualities requirements are met. Subsequently, the linear controller calculates commanded values of the angular and linear accelerations, which serve as virtual inputs for the dynamic inversion. The controller gains in this step are tuned to optimize reference signal tracking. It should be noted that both aforementioned steps are completely independent of the vehicle. The next two steps involve the actual nonlinear dynamic inversion (NDI) calculation and

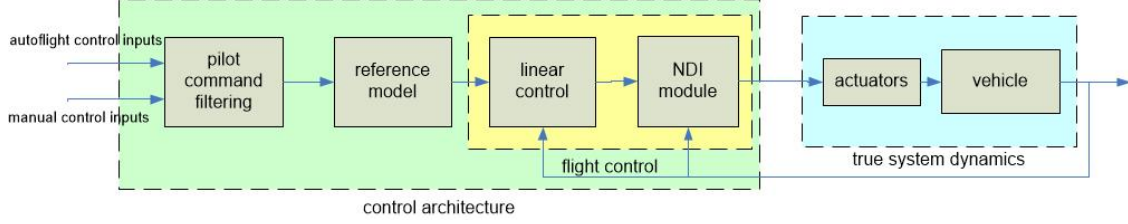


Fig. 3 Global overview of the manual and autoflight control setup

are dependent of the vehicle. In a first step the dynamics are effectively inverted and the three required moments and the required forces are calculated based on the virtual inputs. This calculation requires the mass and inertia, and also the aerodynamic derivatives for regular NDI. Finally, the control allocation step maps the required moments and forces to required thrust values for each propeller, by using the geometry of the vehicle and the thrust angle of each propeller, and to the required control surface deflections, by using their respective control efficiencies.

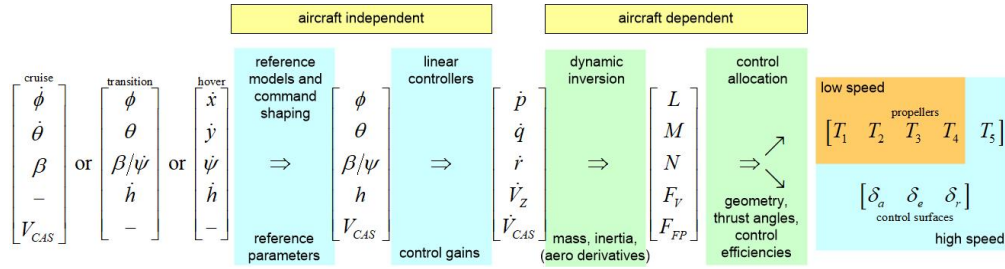


Fig. 4 Overview of different control steps and the relevant quantities

A. Model Inversion

1. NDI control

The required moments and forces are calculated as follows[5]:

$$\begin{bmatrix} L_{\text{req}} \\ M_{\text{req}} \\ N_{\text{req}} \\ F_{\text{vert req}} \\ F_{\text{flightpath req}} \end{bmatrix} = \begin{bmatrix} I_{XX}\dot{p}_{\text{req}} - I_{XZ}\dot{r}_{\text{req}} - q(I_{XZ}p - I_{ZZ}r) - I_{YY}qr - C_l(\beta, p, r)\bar{q}Sb \\ I_{YY}\dot{q}_{\text{req}} + r(I_{XX}q - I_{XZ}r) + p(I_{XZ}p - I_{ZZ}r) - C_m(\alpha, q, \delta_{\text{fl}})\bar{q}S\bar{c} \\ I_{ZZ}\dot{r}_{\text{req}} - I_{XZ}\dot{p}_{\text{req}} - q(I_{XX}p - I_{XZ}r) + I_{YY}pq - C_n(\beta, p, r)\bar{q}Sb \\ \frac{m(g + \dot{V}_{Z\text{req}})}{\cos \phi} - (C_L\bar{q}S)\cos \gamma \\ m(\dot{V}_{\text{req}} + g \sin \gamma) + (C_D\bar{q}S) \end{bmatrix} \quad (26)$$

with the aerodynamic contributions $C_l(\beta, p, r)$, $C_m(\alpha, q, \delta_{\text{fl}})$ and $C_n(\beta, p, r)$ defined as in Eq. (12).

2. INDI control

Based on the principles of Incremental NDI, as outlined in Sec. III.B, the equation for the required moments and forces (26) in Sec. IV.A.1 is rewritten and simplified[5]:

$$\begin{bmatrix} dL_{\text{req}} \\ dM_{\text{req}} \\ dN_{\text{req}} \\ dF_{\text{vert req}} \\ dF_{\text{flightpath req}} \end{bmatrix} = \begin{bmatrix} I_{XX}(\dot{p}_{\text{req}} - \hat{p}_0) - I_{XZ}(\dot{r}_{\text{req}} - \hat{r}_0) \\ I_{YY}(\dot{q}_{\text{req}} - \hat{q}_0) \\ I_{ZZ}(\dot{r}_{\text{req}} - \hat{r}_0) - I_{XZ}(\dot{p}_{\text{req}} - \hat{p}_0) \\ \frac{m}{\cos \phi}(\dot{V}_{Z\text{req}} - \hat{V}_{Z0}) \\ m(\dot{V}_{\text{req}} - \hat{V}_0) \end{bmatrix} \quad (27)$$

By comparing Eq. (27) with (26), one can see that for INDI only mass and inertial properties are needed. No aerodynamic properties are needed for calculating the required forces and moments with INDI, contrary to the conventional NDI approach. This is a significant advantage for the class of vehicles as studied in this paper, because it is assumed that no detailed aerodynamic information of these vehicles will be available.

An important aspect of INDI, however, is the need for filtered signals for previous control commands as well as the state derivatives. The angular and linear accelerations are acquired via differentiating and filtering of the measured angular and linear rates. Filtering is required to limit the noise due to differentiation. The filter is of a second-order low-pass form:

$$H_{\text{fil}}(s) = \frac{\omega_{n_{\text{fil}}}^2}{s^2 + 2\zeta_{\text{fil}}\omega_{n_{\text{fil}}}s + \omega_{n_{\text{fil}}}^2} \quad (28)$$

The same filter is applied on the measurement or model output of the previous control input. Note that care should be taken with selecting the filter coefficients. The estimated accelerations should be sufficiently free of noise such that subsequent noise propagation into the control laws is avoided. Noisy control signals can lead to excessive wear on the actuators and increased likelihood of failure. The filter bandwidth $\omega_{n_{\text{fil}}}$ could be lowered to 80 rad/s before serious performance degradation was observed (especially for compensating for aerodynamic transition effects). The damping ratio ζ_{fil} was set equal to 1.

B. Control allocation

Two versions of control allocation were studied. First algebraic control allocation, discussed in Sec. IV.B.1. During initial testing, it was found that this setup is prone to control saturation, especially for the rotors. Therefore, an alternative prioritized control allocation method was investigated, which makes use of weighted least squares. This concept is discussed in Sec. IV.B.2.

1. Algebraic control allocation

Depending on the flight regime, control allocation calculates the required thrust levels to be provided by the individual propellers, or the required deflections of the relevant control surfaces, in order to achieve certain required moment and/or force values:

$$\begin{bmatrix} T_1 \\ T_2 \\ T_3 \\ T_4 \\ T_5 \end{bmatrix} = \mathcal{M}_{\text{CA}_{\text{prop}}} \setminus \begin{bmatrix} L_{\text{req}} \\ M_{\text{req}} \\ N_{\text{req}} \\ F_{\text{vert req}} \\ F_{\text{flightpath req}} \end{bmatrix} \quad \text{or} \quad \begin{bmatrix} dT_1 \\ dT_2 \\ dT_3 \\ dT_4 \\ dT_5 \end{bmatrix} = \mathcal{M}_{\text{CA}_{\text{prop}}} \setminus \begin{bmatrix} dL_{\text{req}} \\ dM_{\text{req}} \\ dN_{\text{req}} \\ dF_{\text{vert req}} \\ dF_{\text{flightpath req}} \end{bmatrix} \quad \text{with} \quad \begin{bmatrix} T_1 \\ T_2 \\ T_3 \\ T_4 \\ T_5 \end{bmatrix} = \begin{bmatrix} \hat{T}_{1_0} \\ \hat{T}_{2_0} \\ \hat{T}_{3_0} \\ \hat{T}_{4_0} \\ \hat{T}_{5_0} \end{bmatrix} + \begin{bmatrix} dT_1 \\ dT_2 \\ dT_3 \\ dT_4 \\ dT_5 \end{bmatrix} \quad (29)$$

$$\begin{bmatrix} \delta_a \\ \delta_e \\ \delta_r \end{bmatrix} = \mathcal{M}_{\text{CA}_{\text{aero}}} \setminus \begin{bmatrix} L_{\text{req}} \\ M_{\text{req}} \\ N_{\text{req}} \\ F_{\text{vert req}} \\ F_{\text{flightpath req}} \end{bmatrix} \quad \text{or} \quad \begin{bmatrix} d\delta_a \\ d\delta_e \\ d\delta_r \end{bmatrix} = \mathcal{M}_{\text{CA}_{\text{aero}}} \setminus \begin{bmatrix} dL_{\text{req}} \\ dM_{\text{req}} \\ dN_{\text{req}} \\ dF_{\text{vert req}} \\ dF_{\text{flightpath req}} \end{bmatrix} \quad \text{with} \quad \begin{bmatrix} \delta_a \\ \delta_e \\ \delta_r \end{bmatrix} = \begin{bmatrix} \hat{\delta}_{a_0} \\ \hat{\delta}_{e_0} \\ \hat{\delta}_{r_0} \end{bmatrix} + \begin{bmatrix} d\delta_a \\ d\delta_e \\ d\delta_r \end{bmatrix} \quad (30)$$

where \setminus represents the left inverse symbol, the equations on the left apply for regular NDI and on the right for INDI, and with the control allocation matrices for the propellers $\mathcal{M}_{\text{CA}_{\text{prop}}}$ and the control surfaces $\mathcal{M}_{\text{CA}_{\text{aero}}}$ defined as follows:

$$\mathcal{M}_{\text{CA}_{\text{prop}}} = \begin{bmatrix} \eta_{\text{aero} \rightarrow \text{hover}} \cdot \mathcal{M}_{\text{CA}_{\text{propM} \rightarrow \text{T}}} \\ \mathcal{M}_{\text{CA}_{\text{propF} \rightarrow \text{T}}} \end{bmatrix} \quad (31)$$

$$\mathcal{M}_{\text{CA}_{\text{aero}}} = \begin{bmatrix} (1 - \eta_{\text{aero} \rightarrow \text{hover}}) \cdot \mathcal{M}_{\text{CA}_{\text{aeroM} \rightarrow \delta}} \\ \mathbf{0}_{2 \times 3} \end{bmatrix} \quad (32)$$

with each component of these matrices defined as follows:

$$\mathcal{M}_{\text{CApropM} \rightarrow \text{T}} = \begin{bmatrix} dy_f \sin \delta_{T_1} - k_m \cos \delta_{T_1} & -dy_f \sin \delta_{T_2} + k_m \cos \delta_{T_2} & dy_r \sin \delta_{T_3} + k_m \cos \delta_{T_3} & -dy_r \sin \delta_{T_4} - k_m \cos \delta_{T_4} & 0 \\ dx_f \sin \delta_{T_1} + dz_f \cos \delta_{T_1} & dx_f \sin \delta_{T_2} + dz_f \cos \delta_{T_2} & -dx_r \sin \delta_{T_3} - dz_r \cos \delta_{T_3} & -dx_r \sin \delta_{T_4} - dz_r \cos \delta_{T_4} & 0 \\ k_m \sin \delta_{T_1} + dy_f \cos \delta_{T_1} & -k_m \sin \delta_{T_2} - dy_f \cos \delta_{T_2} & -k_m \sin \delta_{T_3} + dy_r \cos \delta_{T_3} & k_m \sin \delta_{T_4} - dy_r \cos \delta_{T_4} & 0 \end{bmatrix} \quad (33)$$

In Eq. (33), k_m is the torque constant of the propellers. Furthermore:

$$\mathcal{M}_{\text{CApropF} \rightarrow \text{T}} = \begin{bmatrix} \eta_{\text{aero} \rightarrow \text{hover}} & 0 \\ 0 & (1 - \eta_{\text{aero} \rightarrow \text{hover}}) \end{bmatrix} \cdot \begin{bmatrix} \sin(\theta + \delta_{T_1}) & \sin(\theta + \delta_{T_2}) & \sin(\theta + \delta_{T_3}) & \sin(\theta + \delta_{T_4}) & 0 \\ \cos(\alpha + \delta_{T_1}) & \cos(\alpha + \delta_{T_2}) & \cos(\alpha + \delta_{T_3}) & \cos(\alpha + \delta_{T_4}) & \cos(\alpha + \delta_{T_5}) \end{bmatrix} \quad (34)$$

and

$$\mathcal{M}_{\text{CAaeroM} \rightarrow \delta} = \begin{bmatrix} C_{l\delta_a} & 0 & C_{l\delta_r} \\ 0 & C_{m\delta_e} & 0 \\ C_{n\delta_a} & 0 & C_{n\delta_r} \end{bmatrix} \quad (35)$$

The four first columns of $\mathcal{M}_{\text{CApropF} \rightarrow \text{T}}$ allocate the control action to the vertical hover propellers. The last column assigns the control activity to the forward facing cruise propeller. The matrix $\mathcal{M}_{\text{CAaeroM} \rightarrow \delta}$ for the control surfaces is set with the assumption that the symmetric and anti-symmetric control surfaces are decoupled. A full matrix of nonzero elements is needed if this is not the case.

2. Prioritized control allocation

Thrust control saturation is a crucial constraint in this control setup. Especially for aerial vehicles with coupled control effectors, such as this vehicle, actuator saturation may lead to undesired behavior and even loss of control. With the unprioritized control allocation scheme as given in Eq. (29)–(30), it may be that the desired combination of pitching, rolling and yawing moment together with vertical force is not achievable due to maximum or minimum thrust limitations of the propellers and/or due the maximum deflection limits of the control surfaces. In absence of an adequate control allocation algorithm, it is left to chance which one (or combination) of the four objectives will be affected. However, for the flight stability of these multirotor vehicles, it is crucial to apply the full required pitch and roll moments before anything else [27]. Thereafter, the vertical force for altitude control comes in the second place, followed by the yawing moment which is the least essential from a safety point of view. Therefore, a control allocation algorithm is needed that prioritizes the control objectives of roll and pitch over altitude, and subsequently over yaw, and that calculates the required thrust levels per rotor accordingly. Multiple control allocation algorithms have been proposed, some of which do not adequately address prioritization: ganging, redistributed pseudo-inverse, direct control allocation. Others do address prioritization, such as linear programming and quadratic programming [28]. This paper considers a quadratic cost function, and the corresponding quadratic optimization problem. A solution to this problem can be found in a straightforward way using the active set method, as shown by Ref. [29].

In this paper, the Weighted Least Squares (WLS) control allocation algorithm is integrated into the aforementioned dynamic inversion based attitude, altitude and airspeed controller. This chosen control allocation algorithm solves the weighted, bounded least-squares problem by means of the cost function that makes a trade off between the actual input commands \mathbf{u} and the virtual commands \mathbf{v} :

$$\min \|\mathbf{W}_u (\mathbf{u} - \mathbf{u}_d)\|^2 + \gamma \|\mathbf{W}_v (\mathbf{B}\mathbf{u} - \mathbf{v})\|^2 \quad (36)$$

subject to: $\mathbf{u}_{\min} \leq \mathbf{u} \leq \mathbf{u}_{\max}$, where \mathbf{B} is the control effectiveness matrix, \mathbf{v} is the commanded virtual control, \mathbf{u}_{\min} and \mathbf{u}_{\max} are the lower and upper position limits, \mathbf{W}_v is the virtual control weighting matrix which cannot become rank deficient, \mathbf{W}_u is the control weighting matrix which cannot become rank deficient, \mathbf{u}_d is the desired control and finally γ is the weighting between the relative importance of actual control \mathbf{u} and virtual control \mathbf{v} in the overall cost function.

In this control allocation algorithm, the different control effectiveness matrices as defined in Eq. (31) – (35) are combined in one overall control allocation matrix which serves as the control effectiveness matrix \mathbf{B} in Eq. (36):

$$\mathcal{M}_{\text{CA}} = \begin{bmatrix} \mathcal{M}_{\text{CAprop}} & \mathcal{M}_{\text{CAaero}} \end{bmatrix} = \begin{bmatrix} \eta_{\text{aero} \rightarrow \text{hover}} \cdot \mathcal{M}_{\text{CApropM} \rightarrow \text{T}} & (1 - \eta_{\text{aero} \rightarrow \text{hover}}) \cdot \mathcal{M}_{\text{CAaeroM} \rightarrow \delta} \\ \mathcal{M}_{\text{CApropF} \rightarrow \text{T}} & \mathbf{0}_{2 \times 3} \end{bmatrix} \quad (37)$$

The virtual control inputs are $\mathbf{v}_{\text{NDI}} = [L_{\text{req}} \ M_{\text{req}} \ N_{\text{req}} \ F_{\text{vert req}} \ F_{\text{flightpath req}}]^T$ for NDI and $\mathbf{v}_{\text{INDI}} = [dL_{\text{req}} \ dM_{\text{req}} \ dN_{\text{req}} \ dF_{\text{vert req}} \ dF_{\text{flightpath req}}]^T$ for INDI. The control inputs are $\mathbf{u} = [T_1 \ T_2 \ T_3 \ T_4 \ T_5 \ \delta_a \ \delta_e \ \delta_r]^T$. The scalar weight is

the default value $\gamma = 10^{-6}$, but the values of all other parameters in Eq. (36) depend on the configuration and flight condition. For the virtual control weighting matrix \mathbf{W}_v , in hover the highest priority should be given to pitch and roll, followed by altitude and finally yaw[27]. As a consequence, the relevant weighting matrix \mathbf{W}_v is defined as: $\mathbf{W}_v = \text{diag}(1000, 1000, 1, 100, 100)$. In forward flight, all these axes are equally important but altitude is replaced by airspeed along the flightpath: $\mathbf{W}_v = \text{diag}(1, 1, 1, 1, 1)$. Also \mathbf{u}_{\min} and \mathbf{u}_{\max} are adjusted based on which control effectors are effective in each flight condition: in hover $\delta_{\bullet \min} = 0$ and $\delta_{\bullet \max} = 0$, and in forward flight $T_{\bullet \min} = 0$ and $T_{\bullet \max} = 0$. The desired control \mathbf{u}_d enforces a minimum control effort and is zero for the control surface deflections in all flight conditions and for the thrust in forward flight. For hover and transitions, the desired thrust for the vertical rotors is the trim thrust: $T_{\bullet \text{trim}} = \frac{mg}{\cos(\phi) \cos(\theta) n_{\text{eng}}}$. It was found that this avoids differential thrust settings per rotor in certain trim conditions, where all rotors should provide the same thrust levels. The control weighting matrix normalizes the control authority range of all the control effectors: $\mathbf{W}_u = \text{diag}(\mathbf{u}_{\max} - \mathbf{u}_{\min})^{-1}$, so that the total control effort is efficiently distributed over the different control effectors.

The local upper and lower bounds of the control effectors at any given time step are the most restrictive of the local rate and position limits, and are defined as follows for regular NDI and INDI:

NDI:

$$\mathbf{u}_{\min} = \begin{bmatrix} \max(T_{\bullet \min}, T - \dot{T}_{\max} \cdot \Delta t) \\ \max(\delta_{\bullet \min}, \delta - \dot{\delta}_{\max} \cdot \Delta t) \end{bmatrix} \quad (38)$$

$$\mathbf{u}_{\max} = \begin{bmatrix} \min(T_{\bullet \max}, T + \dot{T}_{\max} \cdot \Delta t) \\ \min(\delta_{\bullet \max}, \delta + \dot{\delta}_{\max} \cdot \Delta t) \end{bmatrix} \quad (39)$$

INDI [13]:

$$d\mathbf{u}_{\min} = \begin{bmatrix} \max(T_{\bullet \min} - T, -\dot{T}_{\max} \cdot \Delta t) \\ \max(\delta_{\bullet \min} - \delta, -\dot{\delta}_{\max} \cdot \Delta t) \end{bmatrix} \quad (40)$$

$$d\mathbf{u}_{\max} = \begin{bmatrix} \min(T_{\bullet \max} - T, +\dot{T}_{\max} \cdot \Delta t) \\ \min(\delta_{\bullet \max} - \delta, +\dot{\delta}_{\max} \cdot \Delta t) \end{bmatrix} \quad (41)$$

The desired control \mathbf{u}_d is limited by the local upper and lower bounds of the control effectors for NDI. This requires a re-formulation for INDI since the preference vector refers to a desired actuator position increment $d\mathbf{u}_d$ for INDI [13]. If the preferred increment is set to $d\mathbf{u}_d = 0$, the actuators are forced to remain at a constant, possibly nonzero position whenever it is possible. It has been observed that this can lead to complementary actuators (those producing moments of equal magnitude but opposite sign) diverging to asymmetric nonzero inputs while still producing no net moment. To avoid this situation and to minimize control effort, the control effectors must be driven to their preferred position whenever it is possible. Thus, the preferred position increment at each time step must correspond to the increment that brings the actuators closest to their preferred absolute positions. This is achieved by calculating the incremental desired input vector $d\mathbf{u}_d$ at each time step as defined in Eq. (44).

NDI:

$$\mathbf{u}_d = \begin{bmatrix} T_{\bullet} = T_{\bullet \text{trim}} \\ \delta_{\bullet} = 0 \end{bmatrix} \quad (42)$$

$$\text{with : } \mathbf{u}_{\min} \leq \mathbf{u}_d \leq \mathbf{u}_{\max} \quad (43)$$

INDI:

$$d\mathbf{u}_d = \mathbf{u}_d - \mathbf{u} \quad (44)$$

$$\text{with : } d\mathbf{u}_{\min} \leq d\mathbf{u}_d \leq d\mathbf{u}_{\max} \quad (45)$$

The changes in the parameters for the prioritized control allocation algorithm across flight regimes are summarized in Table 3.

Table 3 PCA parameters per flight regime

parameter	hover	transition	forward flight
\mathbf{W}_v	$\text{diag}(1000, 1000, 1, 100, 100)$	$\text{diag}(1000, 1000, 1, 100, 100)$	$\text{diag}(1, 1, 1, 1, 1)$
\mathbf{W}_u	$\text{diag}(\mathbf{u}_{\max} - \mathbf{u}_{\min})^{-1}$	$\text{diag}(\mathbf{u}_{\max} - \mathbf{u}_{\min})^{-1}$	$\text{diag}(\mathbf{u}_{\max} - \mathbf{u}_{\min})^{-1}$
$\mathbf{u}_{\min}/d\mathbf{u}_{\min}$	$T_{\bullet \min} \neq 0, \delta_{\bullet \min} = 0$	$T_{\bullet \min} \neq 0, \delta_{\bullet \min} \neq 0$	$T_{\bullet \min} = 0, \delta_{\bullet \min} \neq 0$
$\mathbf{u}_{\max}/d\mathbf{u}_{\max}$	$T_{\bullet \max} \neq 0, \delta_{\bullet \max} = 0$	$T_{\bullet \max} \neq 0, \delta_{\bullet \max} \neq 0$	$T_{\bullet \max} = 0, \delta_{\bullet \max} \neq 0$
$\dot{\mathbf{u}}_{\max}$	$\dot{T}_{\bullet \max} \neq 0, \dot{\delta}_{\bullet \max} = 0$	$\dot{T}_{\bullet \max} \neq 0, \dot{\delta}_{\bullet \max} \neq 0$	$\dot{T}_{\bullet \max} = 0, \dot{\delta}_{\bullet \max} \neq 0$
\mathbf{u}_d	$T_{\bullet d} = T_{\bullet \text{trim}}, \delta_{\bullet d} = 0$	$T_{\bullet d} = T_{\bullet \text{trim}}, \delta_{\bullet d} = 0$	$T_{\bullet d} = 0, \delta_{\bullet d} = 0$

This problem was solved using an active set method [29]. The algorithm works as elaborated in Alg. 1.

Initialization: $\mathbf{W} = \{\emptyset\}$, $\mathbf{u}^0 = (\mathbf{u}_{\max} - \mathbf{u}_{\min})/2$, $\mathbf{d} = \mathbf{b} - \mathbf{A}\mathbf{u}^0$, $\mathbf{S} = [\emptyset]$

for $i = 0, 1, 2, \dots, n_{\max}$ **do**

Determine the free column in \mathbf{A} :

$$\mathbf{A}_f = \mathbf{A}(:, h), \quad h \notin \mathbf{W} \quad (46)$$

Determine the optimal perturbation by solving the following least squares problem for \mathbf{p}_f :

$$\mathbf{d} = \mathbf{A}_f \mathbf{p}_f \quad (47)$$

Now \mathbf{p} is constructed from \mathbf{p}_f with zeros for the elements that are in \mathbf{W} .

if $\mathbf{u}^i + \mathbf{p}$ *is feasible* **then**

$$\mathbf{u}^{i+1} = \mathbf{u}^i + \mathbf{p} \text{ and } \mathbf{d} = \mathbf{d} - \mathbf{A}_f \mathbf{p}_f$$

The gradient and Lagrange multipliers are computed with:

$$\nabla = \mathbf{A}^T \mathbf{d} \text{ and } \lambda = \mathbf{S} \nabla \quad (48)$$

if *all* $\lambda \geq 0$ **then**

| The solution \mathbf{u}^{i+1} is optimal: $\mathbf{u} = \mathbf{u}^{i+1}$

else

| The constraint associated with the most negative λ has to be removed from the active set \mathbf{W} .

| Re-iterate with this updated active set.

end

else

The current solution violates a constraint which is not in \mathbf{W} . Determine the maximum factor α such that $\alpha \mathbf{p}$ is a feasible perturbation, with $0 \leq \alpha < 1$. Update the residual \mathbf{d} and the solution \mathbf{u}^{i+1} :

$$\mathbf{u}^{i+1} = \mathbf{u}^i + \alpha \mathbf{p} \quad (49)$$

$$\mathbf{d} = \mathbf{d} - \mathbf{A}_f \alpha \mathbf{p}_f \quad (50)$$

Finally, update the active set and store the sign of the constraint: $S_{jj} = \text{sign}(\mathbf{p}_j)$ with j the index of the new active constraint.

end

end

Algorithm 1: Active set method for WLS problem [27]

C. Linear controllers

Because of the relative degree of two*, the linear controllers work up to the second order time derivative, and they consist of the following control law for roll and pitch:

$$\begin{aligned} v_p &= \dot{p}_{\text{req}} \approx \ddot{\phi}_{\text{req}} \\ &\approx (\eta_{\text{ACAH}} + \eta_{\text{RCAH}} + \eta_{\text{TRC}}) \left(\left(K_\phi + \frac{K_{\phi_I}}{s} \right) (\phi_{\text{comm}} - \phi) + K_{\dot{\phi}} (\dot{\phi}_{\text{comm}} - \dot{\phi}) + K_{\ddot{\phi}} (\ddot{\phi}_{\text{comm}}) \right) \end{aligned} \quad (51)$$

$$\begin{aligned} v_q &= \dot{q}_{\text{req}} \approx \ddot{\theta}_{\text{req}} \cos \phi \\ &\approx (\eta_{\text{ACAH}} + \eta_{\text{RCAH}} + \eta_{\text{TRC}}) \left(\left(K_\theta + \frac{K_{\theta_I}}{s} \right) (\theta_{\text{comm}} - \theta) + K_{\dot{\theta}} (\dot{\theta}_{\text{comm}} - \dot{\theta}) + K_{\ddot{\theta}} (\ddot{\theta}_{\text{comm}}) \right) \cos \phi \end{aligned} \quad (52)$$

The control law for yaw is slightly different and depends on the selected mode:

$$\begin{aligned} v_{r_{\text{RCDH}}} &= \dot{r}_{\text{req}_{\text{RCDH}}} \approx \ddot{\psi}_{\text{req}_{\text{RCDH}}} \cos \phi \cos \theta \\ &\approx (\eta_{\text{RCDH}} + \eta_{\text{DH}}) \left(K_\psi (\psi_{\text{comm}} - \psi) + K_{\dot{\psi}} (\dot{\psi}_{\text{comm}} - \dot{\psi}) + K_{\ddot{\psi}} (\ddot{\psi}_{\text{comm}}) \right) \cos \phi \cos \theta \end{aligned} \quad (53)$$

$$v_{r_{\text{TC}}} = \dot{r}_{\text{req}_{\text{TC}}} = \eta_{\text{TC}} K_r (r_{\text{comm}} - r) \quad (54)$$

*The relative degree of a system is the number of times one has to differentiate the output y before the input u appears explicitly.

Table 4 Linear controller gains for Eq. (51)–(54)

axis	angle	rate	acceleration
roll & pitch	$K_{\phi/\theta} = 5$	$K_{\dot{\phi}/\dot{\theta}} = 5$	$K_{\ddot{\phi}/\ddot{\theta}} = 1$
	$K_{\phi_I/\theta_I} = 3$		
yaw	$K_{\psi} = 0.75$	$K_{\dot{\psi}} = 2.5$	$K_{\ddot{\psi}} = 1$
	–	$K_r = 2$	–
vertical	$K_h = 0.8$	$K_{\dot{h}} = 2$	$K_{\ddot{h}} = 1$

Table 5 Reference model parameters for Eq. (56)

axis	damping ratio	natural frequency
roll & pitch	$\zeta_{\phi/\theta} = 0.8$	$\omega_{n_{\phi/\theta}} = [1.4 - 2.4] \text{ rad/s}$
yaw & altitude	$\zeta_{\psi/h} = 0.8$	$\omega_{n_{\psi/h}} = 0.67 \text{ rad/s}$

Eq. (53) applies for the rate command direction hold (RCDH) mode (section IV.E.3), which tracks the heading ψ , and Eq. (54) is used for the turn coordination (TC) mode (section IV.E.6), which tracks the sideslip angle β . Finally, the control law for the vertical speed is as follows:

$$\nu_{\dot{z}} = \ddot{z}_{\text{req}} = (\eta_{\text{RCHH}} + \eta_{\text{AH}}) \left(K_h (h_{\text{comm}} - h) + K_{\dot{h}} (\dot{h}_{\text{comm}} - \dot{h}) + K_{\ddot{h}} (\ddot{h}_{\text{comm}}) \right) \quad (55)$$

The values of the controller gains mentioned in Eq. (51)–(55) are specified in Table 4. The first and second order time derivatives of the control commands used in Eq. (51)–(52) are fed forward internal signals from the second order reference models discussed in Sec. IV.D. Integral action is added in the first term of these linear control laws, in order to achieve some robustness with respect to model inaccuracies in the inversion model [20]. The mode blending factors η_{\bullet} vary between 0 and 1 for discrete mode transitions and depend on which modes are active.

D. Reference model

The reference models for the roll, pitch, yaw and altitude channels are of the second order:

$$H_{\text{ref}}(s) = \frac{\omega_{n_{\text{ref}}}^2}{s^2 + 2\zeta_{\text{ref}}\omega_{n_{\text{ref}}}s + \omega_{n_{\text{ref}}}^2} \quad (56)$$

The parameter values for Eq. (56) are defined in Table 5 and were chosen such that the reference model satisfies the ADS-33 Flying and Handling Quality requirements, as discussed in Ref. [5]. Besides, faster responses are needed in forward flight, which results in a configuration based blending of the reference frequencies in Eq. (56). Furthermore, these reference models will be instrumental for future work, which will include pseudo control hedging[30–33] and safe flight envelope protections[34–37]. Both previously developed techniques must be adapted for this class of vehicles.

E. Pilot Command Filtering

This class of vehicles is a hybrid between a rotary and a fixed wing aircraft, making the pilot command filtering unconventional. Depending on the flight condition, specific command filtering strategies are needed. Fig. 5 shows how they are related to the flap handle. In the hover and low speed flight phases, the vehicle relies on differential RPM for attitude control and collective RPM for altitude control. At higher airspeeds the dynamic pressure becomes larger such that the flight control surfaces become effective and can gradually take over control authority for attitude control and ultimately altitude control.

Fig. 6 shows how the different command filtering modes for stick, pedals and collective work and how they interact. The stick commands bank ϕ and pitch attitude θ angles directly during the hover and low speed flight phases, using the Attitude Command Attitude Hold (ACAH) mode. For landing and precision maneuvering with respect to the ground, an add-on mode is used which is called Translational Rate Command (TRC). Using this mode, the pilot has direct

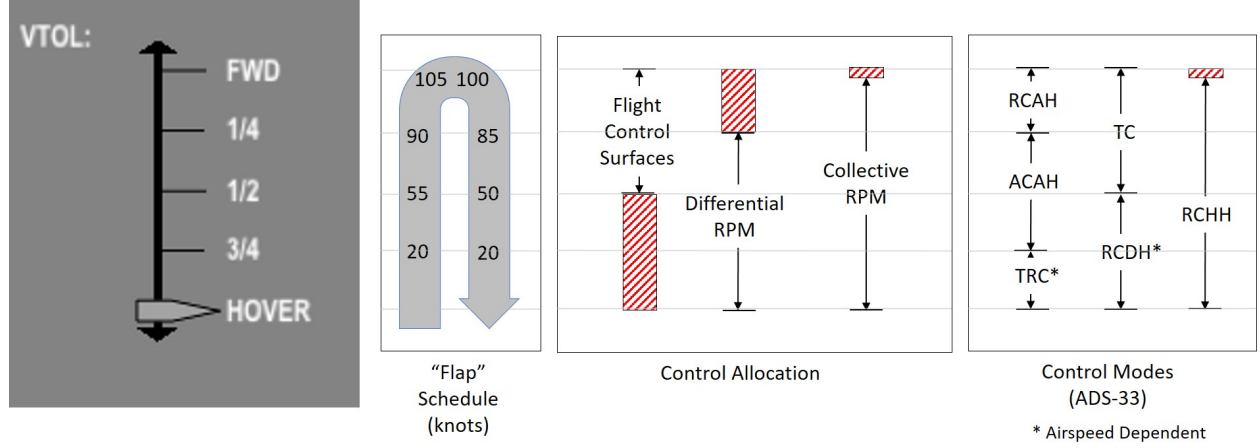


Fig. 5 Flap handle converted to specify hover/forward flight transition control configurations

control over longitudinal and lateral inertial speed components u_N, v_N through the stick. For cruise flight at higher airspeeds, the system switches to Rate Command Attitude hold (RCAH), which connects the stick to the angular rates $\dot{\phi}, \dot{\theta}$. The pedals are used for yaw control. During hover and landing, and flight at low airspeeds, the pedals command a rate of change in the heading ψ through the Rate Command Direction Hold (RCDH) mode. For flight at higher airspeeds, this changes into a Turn Coordination (TC) mode, which allows the pedals to control the sideslip angle β , for example in case of a decrab maneuver during a conventional fixed-wing landing on a runway. Finally, the collective controls the sink or climb rate through the Rate Command Height Hold (RCHH) mode, as long as the collective RPM mode is active.

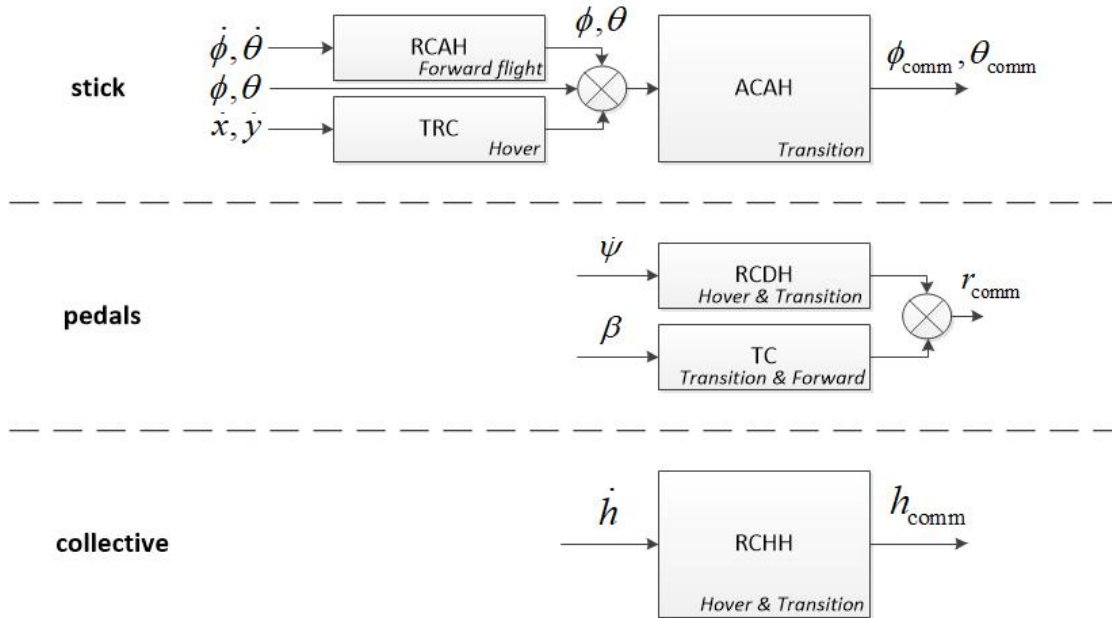


Fig. 6 Different command filtering modes for stick, pedals and collective

For all these modes except ACAH, additional command filtering is needed. The RCAH, RCDH and RCHH modes include an integrator, such that they all become rate command attitude/direction/altitude hold modes[20]. Each of these modes is discussed in more detail next.

1. Attitude Command Attitude Hold (ACAH)

Attitude command attitude hold is the most straightforward command mode, as the stick inputs are directly connected to the reference models in Sec. IV.D. Longitudinal stick inputs command the pitch attitude and lateral stick inputs command the roll attitude. This mode is mostly used in transition flight phases. Fig. 7 illustrates the interconnection between reference model and controller for this control mode. The rate and acceleration feedforward signals from reference model to linear controller minimize lag between response and reference signal.

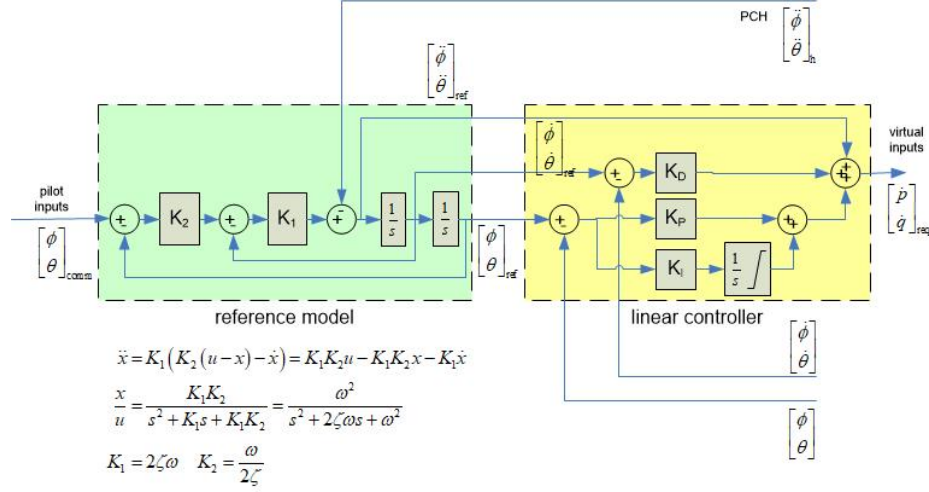


Fig. 7 Block diagram of reference model and linear controller for attitude command attitude hold (ACAH)

2. Rate Command Attitude Hold (RCAH)

Rate command attitude hold is a variation of ACAH, where longitudinal and lateral stick deflections command inertial pitch and roll rates respectively. This mode is used in the cruise forward flight phase. This command filtering consists of an integrator, of which the output is connected to the reference models in Sec. IV.D. This mode allows the pilot to release the stick and the vehicle will maintain the same attitude. Even in case of external disturbances, like turbulence or wake, the vehicle will return to its reference attitude. Fig. 8 illustrates the interconnections between pilot command filtering, reference model and controller for this control mode. The aforementioned rate and acceleration feedforward signals between reference model and linear controller are still preserved, and another rate feedforward signal is included from the command filtering to the reference model, for the same purpose of lag minimization. The rate feedforward signal is switched off when the integrator reaches saturation limits.

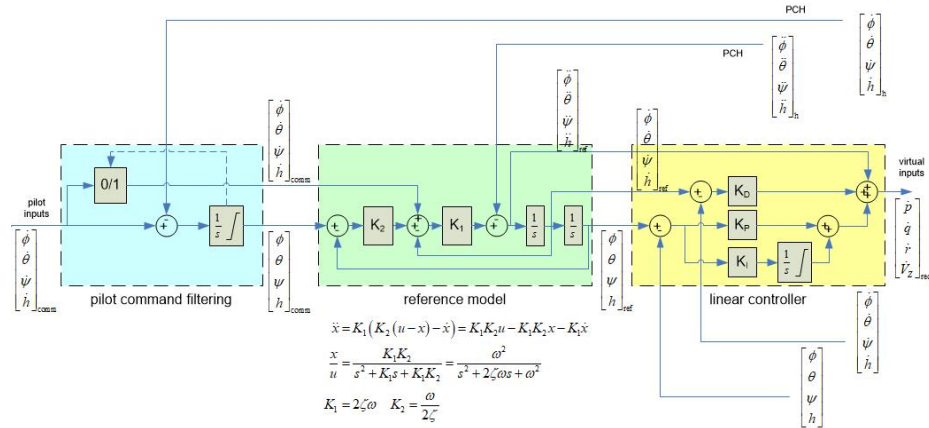


Fig. 8 Block diagram of command filtering, reference model and linear controller for rate command attitude hold (RCAH)

3. Rate Command Direction Hold (RCDH)

Rate command direction hold is similar to RCAH. A steady pedal deflection commands a steady rate of change of the heading. This mode is used in the hover and landing phases of flight. This command filtering consists of an integrator as well, of which the output is connected to the reference model of the yaw channel in Sec. IV.D. This mode allows the pilot to release the pedals and the vehicle will maintain the same heading.

4. Rate Command Height Hold (RCHH)

Rate command height hold is similar to the both previous ones. A steady collective deflection commands a steady climb or sink rate. This mode is used in all phases of flight where collective RPM is active. This module includes an integrator too, of which the output is connected to the reference model of the vertical speed channel in Sec. IV.D. This mode allows the pilot to release the collective and the vehicle will maintain the same altitude. Even in case of external disturbances, like turbulence or wake, the vehicle will return to its reference altitude.

5. Translational Rate Command (TRC)

Translational Rate Command is a dedicated mode which is used in the landing phase and for precision maneuvering with respect to the ground. Longitudinal and lateral stick deflections command the forward and sideways inertial speed components respectively. The derivation of how these inertial speed components map to the pitch and roll angles is shown below.

This kinematic relationship shows how the translational rate components are related to the Euler angles[38]:

$$\begin{bmatrix} \ddot{x}_{GS} \\ \ddot{y}_{GS} \\ \ddot{z}_{GS} \end{bmatrix} = \begin{bmatrix} 0 \\ 0 \\ g \end{bmatrix} + \frac{1}{m} \mathbf{\Omega}_\psi^{-1} \mathbf{\Omega}_\theta^{-1} \mathbf{\Omega}_\phi^{-1} \left(\begin{bmatrix} \bar{q} SC_{X_B} \\ \bar{q} SC_{Y_B} \\ \bar{q} SC_{Z_B} \end{bmatrix} + \begin{bmatrix} T \cos \delta_T \\ 0 \\ T \sin \delta_T \end{bmatrix} \right) \quad (57)$$

where the body force components are defined by the aerodynamic forces as follows:

$$\begin{bmatrix} \bar{q} SC_{X_B} \\ \bar{q} SC_{Y_B} \\ \bar{q} SC_{Z_B} \end{bmatrix} = \bar{q} S \mathbf{\Omega}_\alpha^{-1} \mathbf{\Omega}_\beta^{-1} \begin{bmatrix} -C_{D_A} \\ C_{Y_A} \\ -C_{L_A} \end{bmatrix} \quad (58)$$

Simplifying by assuming that only the vertical rotors are used in the hover phase and that the aerodynamic influences are negligible due to the low airspeed, results in:

$$m \mathbf{\Omega}_\psi \begin{bmatrix} \ddot{x}_{GS} \\ \ddot{y}_{GS} \\ \ddot{z}_{GS} - g \end{bmatrix} = \mathbf{\Omega}_\theta^{-1} \mathbf{\Omega}_\phi^{-1} \begin{bmatrix} 0 \\ 0 \\ T \sin \delta_T \end{bmatrix} \quad (59)$$

Expanding these matrix equations results in:

$$\begin{bmatrix} m(\ddot{x}_{GS} \cos \psi + \ddot{y}_{GS} \sin \psi) \\ m(\ddot{y}_{GS} \cos \psi - \ddot{x}_{GS} \sin \psi) \\ m(\ddot{z}_{GS} - g) \end{bmatrix} = \begin{bmatrix} \cos \phi \sin \theta T \sin \delta_T \\ -\sin \phi T \sin \delta_T \\ \cos \phi \cos \theta T \sin \delta_T \end{bmatrix} \quad (60)$$

Solving for pitch angle θ and bank angle ϕ results in:

$$\tan \theta = \frac{\ddot{x}_{GS} \cos \psi + \ddot{y}_{GS} \sin \psi}{\ddot{z}_{GS} - g} \quad (61)$$

$$\sin \phi = -\frac{m(\ddot{y}_{GS} \cos \psi - \ddot{x}_{GS} \sin \psi)}{T \sin \delta_T} \quad (62)$$

Besides it can be found that:

$$m \left\| \begin{bmatrix} \ddot{x}_{GS} \\ \ddot{y}_{GS} \\ \ddot{z}_{GS} - g \end{bmatrix} \right\|_2 = \left\| \begin{bmatrix} 0 \\ 0 \\ T \sin \delta_T \end{bmatrix} \right\|_2 \quad (63)$$

Table 6 Linear controller gains for Eq. (67)–(69)

axis	rate	acceleration
longitudinal & lateral	$K_{\dot{x}/\dot{y}/\dot{z}} = 2 * 0.25$ $K_{\ddot{x}/\ddot{y}/\ddot{z}} = 0.25^2$	$K_{\ddot{x}/\ddot{y}} = 1$

And thus:

$$T \sin \delta_T = m \sqrt{\ddot{x}_{GS}^2 + \ddot{y}_{GS}^2 + (\ddot{z}_{GS} - g)^2} \quad (64)$$

Implementing Eq. (64) in Eq. (62) results in the following equations for required pitch attitude and bank angles based on the required translational accelerations, and which are independent of any airframe information:

$$\theta_{\text{req}} = \arctan \frac{\ddot{x}_{GS_{\text{req}}} \cos \psi + \ddot{y}_{GS_{\text{req}}} \sin \psi}{\ddot{z}_{GS_{\text{req}}} - g} \quad (65)$$

$$\phi_{\text{req}} = -\arcsin \frac{(\ddot{y}_{GS_{\text{req}}} \cos \psi - \ddot{x}_{GS_{\text{req}}} \sin \psi)}{\sqrt{\ddot{x}_{GS_{\text{req}}}^2 + \ddot{y}_{GS_{\text{req}}}^2 + (\ddot{z}_{GS_{\text{req}}} - g)^2}} \quad (66)$$

Because of the relative degree, the linear controllers of the two TRC channels work up to the second order derivative, and they have the following control law:

$$v_{\ddot{x}} = \ddot{x}_{GS_{\text{req}}} = \left(K_{\dot{x}} + \frac{K_{\ddot{x}_I}}{s} \right) (\dot{x}_{GS_{\text{ref}}} - \dot{x}_{GS}) + K_{\ddot{x}} (\ddot{x}_{GS_{\text{ref}}}) \quad (67)$$

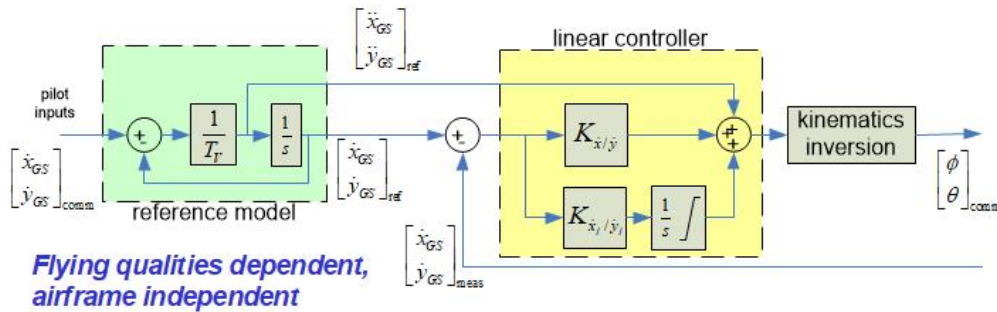
$$v_{\ddot{y}} = \ddot{y}_{GS_{\text{req}}} = \left(K_{\dot{y}} + \frac{K_{\ddot{y}_I}}{s} \right) (\dot{y}_{GS_{\text{ref}}} - \dot{y}_{GS}) + K_{\ddot{y}} (\ddot{y}_{GS_{\text{ref}}}) \quad (68)$$

$$v_{\ddot{z}} = \ddot{z}_{GS_{\text{req}}} = K_{\dot{z}} (\dot{z}_{GS_{\text{ref}}} - \dot{z}_{GS}) \quad (69)$$

The values of the controller gains mentioned in Eq. (67)–(69) are specified in Table 6. The second order time derivatives of the control commands used in Eq. (67)–(69) are fed forward internal signals from the first order reference models for the two TRC channels:

$$H_{\text{ref}}(s) = \frac{1}{T_V s + 1} \quad (70)$$

The value for the time constant in Eq. (70) is $T_V = 3s$ and was chosen such that the reference model satisfies the ADS-33 Flying and Handling Quality requirements, as discussed in Sec. V.C.

**Fig. 9 Detailed overview of the control structure and interconnections for TRC (translational rate control)**

6. Turn Coordination (TC)

For turn coordination, sideslip β control has been implemented as outer loop over rate control according to the following control law[20]:

$$r_{\text{comm}} = -K_{\beta} (\beta_{\text{comm}} - \beta) + \frac{g \sin \phi \cos \theta}{V} \quad (71)$$

where the controller gain $K_{\beta} = 0.5$. This commanded yaw rate r_{comm} is then implemented in Eq. (54).

F. Pseudo Control Hedging (PCH)

The concept of Pseudo Control Hedging (PCH) was initially developed by Johnson.[30, 39] Aim is to compensate the reference model signal for input characteristics such as actuator position limits, actuator rate limits, and linear input dynamics. In the work of Holzapfel, see Ref. [31, 32], this concept has been applied in an adaptive control setup based upon nonlinear dynamic inversion. An additional advantage of PCH is that the relative order of the dynamic inversion operation can be reduced by one degree. NDI inverts the aircraft dynamics, but not the input behavior, represented by the actuators. The use of PCH provides an alternative for an eventual additional inversion loop for these dynamics. It was found that input saturation is a concern for nonlinear dynamic inversion based control, and it is also relevant for this class of eVTOL vehicles. This topic is part of currently ongoing research.

G. Overview of the closed loop system

Fig. 10 shows the detailed overview how all the previously discussed blocks are interconnected in the closed loop system. The aircraft model currently studied in this paper involves thrust control over the five propellers as well as the control surfaces, as illustrated in Fig. 10. The model inversion and control allocation blocks in Fig. 10 are specified by Eq. (26) (NDI model inversion) or Eq. (27) (INDI model inversion) and Eq. (36) (control allocation). These modules are the only airframe dependent part of the overall control law, where values for the mass, inertia, geometry, thrust angles, torque coefficient, control efficiencies and aero (NDI only) parameters are needed. The linear control module in Fig. 10 is specified by Eq. (52)–(55) and the reference models are defined in Eq. (56). Both are airframe independent, but flying and handling qualities dependent. The reference model parameters are tuned to satisfy the ADS-33 flying and handling quality requirements, and the linear controller parameters in Eq. (52)–(55) are tuned for reference signal tracking. This decoupled control setup simplifies controller parameter tuning significantly. Fig. 10 also shows the feedforward channels for reference angular rates and accelerations from reference model to linear controller, further simplifying signal handling.

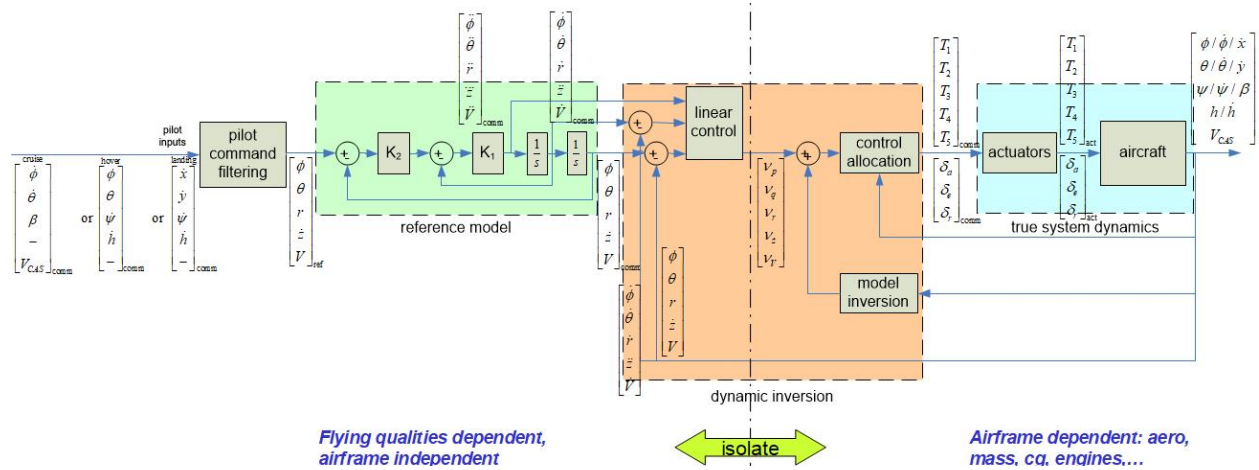


Fig. 10 Detailed overview of the control structure and interconnections

V. Simulation results of the nonlinear controller

Three sets of simulation results are presented. Section V.A shows a short demonstration flight in the urban environment of San Francisco. Section V.B discusses a longer demonstration flight from San Francisco International Airport to San Francisco. Section V.C verifies if the translational rate command system complies with the ADS-33 requirements. All the results presented here are obtained with incremental nonlinear dynamic inversion (INDI) and prioritized control allocation with weighted least squares, unless stated otherwise. Overall, it was observed that the performance differences between NDI and INDI were negligible for the examples studied here.

A. Sample demo flight plan in downtown San Francisco

Fig. 11 shows the map and the 3D trajectory of a sample demonstration mission, flown by means of a preprogrammed flightplan in the flight management system. The vehicle takes off vertically from the tip of pier 14 near the ferry building in San Francisco and flies a circuit after which it lands vertically on the rooftop of the parking structure at Mission and 5th.

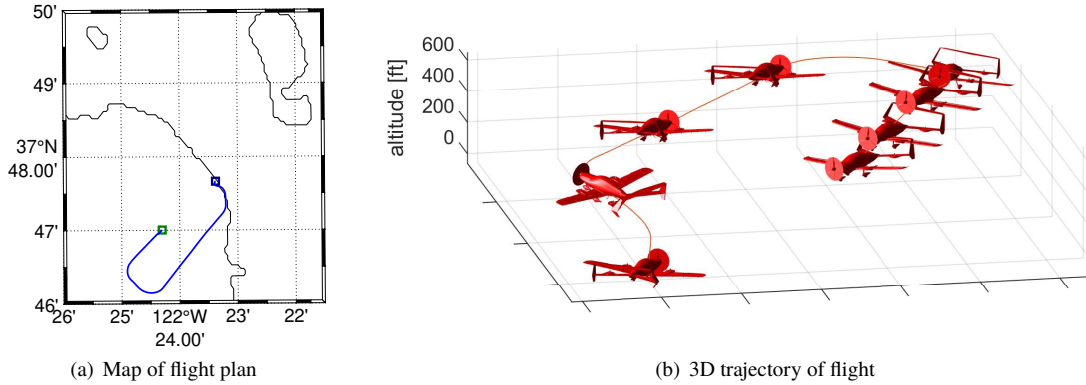


Fig. 11 Map and 3D trajectory of flight plan

Fig. 12 provides more detail on the flight phases of the short demonstration flight. During the initial climb in hover mode, the vehicle yaws to the left with low forward speed. Then it pitches forward to speed up and activates the 5th main propeller to accelerate further, while changing to VTOL mode 3/4. While accelerating, the vehicle starts to bank to the right to heading 203 and accelerates to 60 kts while climbing to 500 ft altitude. Once both are established, the vehicle changes to VTOL mode 1/2. Halfway the circuit, the vehicle makes two consecutive 90 deg turns. The first one is executed at 60 kts, during the second one the vehicle starts to slow down to 30 kts and changes to VTOL mode 3/4. Shortly after, the descent is started at 30 kts. Shortly before altitude capture of 200 ft, the vehicle starts to decelerate towards 20 kts. At this point, hover mode is activated and the 5th main prop is switched off. The vehicle maneuvers towards the landing area, and once it is lined up with the vertiport area, it descends vertically on the rooftop which is at 167 ft. The thicker blue lines in Fig. 12(a) as well as the vertical black dashed lines in Fig. 12(b) illustrate the moments when the VTOL mode changes. Fig. 12(a) shows the 'transition corridor' of the vehicle from hover towards cruise flight condition and vice versa. This flight was performed in a realistic, steady but non-uniform wind field, consistent with the local urban environment. The steady windfield, defined as around 20kts from the East, as shown in Fig. 13, was generated using the commercial CFD solver STAR-CCM+ and a downtown portion of a digital model of San Francisco. [40, 41] The impact of local wind variations along the flightpath is especially visible in the speed variable in Fig. 12. As an example, the 8 kts airspeed after touchdown in Fig. 12(a) is caused by the wind over the rooftop.

Each VTOL mode, as illustrated in Fig. 12, corresponds with their respective control mode and propulsion configuration, as elaborated in Tab. 7. In hover mode, only the 4 vertical rotors T_{1-4} are used, without main rotor T_5 and the control surfaces. Longitudinal and lateral control are established with translational rate command (TRC) for maneuvering accuracy with respect to the ground. Directional and vertical control modes are rate command direction hold (RCDH) and rate command height hold (RCHH) respectively. In VTOL mode 3/4, rotor T_5 is activated, lon and lat control switch to attitude command attitude hold (ACAH), and directional control changes gradually from RCDH towards turn coordination (TC). In mode 1/2 the control surfaces ailerons δ_a , elevators δ_e and rudder δ_r become active. In modes 1/4 and forward, the 4 vertical rotors are gradually switched off since wing-borne flight is established.

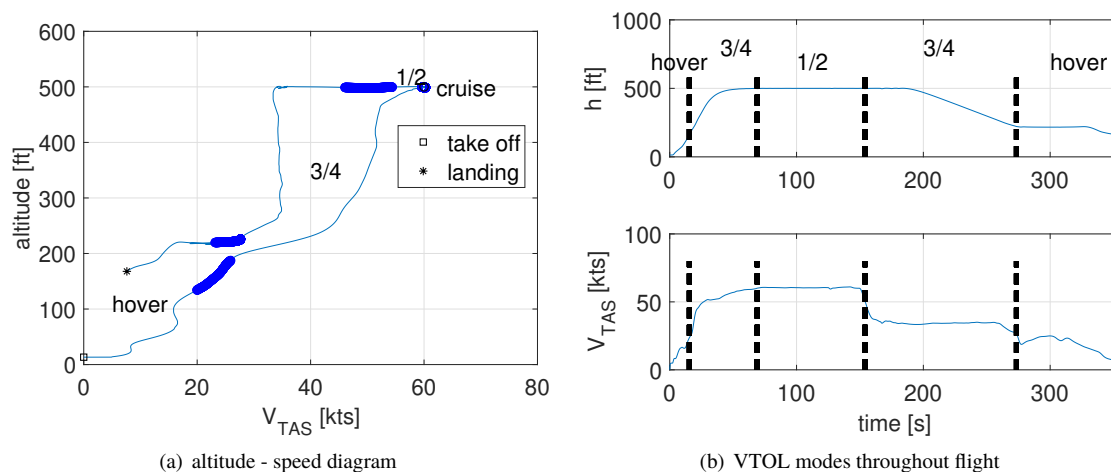


Fig. 12 altitude, speed and VTOL modes throughout the demo flight

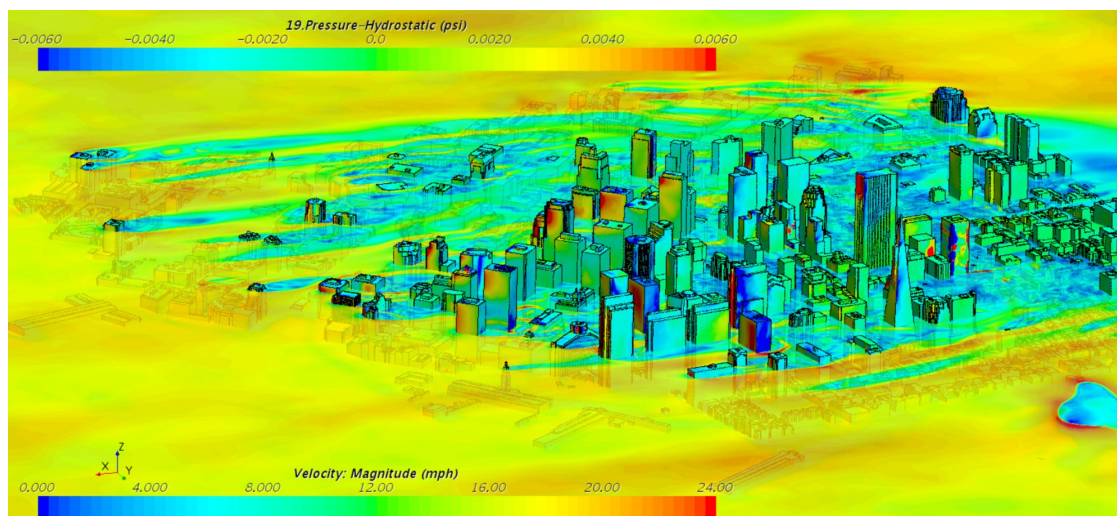


Fig. 13 Steady non-uniform wind field in downtown San Francisco, generated by commercial CFD solver.
Source: NASA Ames Systems Analysis Office

Moreover, lon and lat control is done by means of the conventional rate command attitude hold (RCAH) for fixed wing aircraft. For this short intra-city flight, VTOL modes 1/4 and forward were not achieved.

Table 7 Control modes and propulsion configuration per VTOL mode

VTOL mode		hover	$\frac{3}{4}$	$\frac{1}{2}$	$\frac{1}{4}$	fwd
active controls	T_{1-4}	✓	✓	✓	✓	–
	T_5	–	✓	✓	✓	✓
	$\delta_{a/e/r}$	–	–	✓	✓	✓
lon/lat control	TRC	ACAH	ACAH	ACAH	ACAH	RCAH
dir control	RCDH	RCDH – TC	TC	TC	TC	TC
vert control	RCHH	RCHH	RCHH	RCHH	RCHH	–

The following sections elaborate on the different control modes and their respective control effectors discussed earlier. For the sake of the interpretation of the flight physics, these specific graphs do not consider wind disturbances unless stated otherwise.

1. Attitude Command Attitude Hold

The attitude command attitude hold (ACAH) mode works for two axes, namely longitudinally for pitch, as shown in Fig. 14(a) and laterally for roll, illustrated in Fig. 14(b). Each figure shows the controlled variable on the top, respectively pitch angle θ and roll angle ϕ . In fact, three time histories are shown here, namely the commanded angles, together with their reference values (output of second order reference models), and the vehicle's response. These graphs show good tracking of the commanded values in all VTOL modes. Note that even in the TRC mode during hover, ACAH is still active in an inner loop, as illustrated in Fig. 6. Below the controlled variables, the corresponding inputs are given per axis. Fig. 14(a) shows the longitudinal thrust difference for the four vertical rotors $\Delta T_{lon} = (T_1 + T_2) - (T_3 + T_4)$ and the elevator deflection δ_e , in Fig. 14(b) these are the lateral thrust difference for the four vertical rotors $\Delta T_{lat} = (T_1 + T_3) - (T_2 + T_4)$ and the aileron deflection δ_a . Analyzing these figures shows that only the thrust differences control the vehicle in VTOL modes hover and 3/4, since the control surfaces are not yet effective in these low speed flight conditions. The control surfaces become active in VTOL mode 1/2 and support the four rotors which are becoming less effective at higher speeds. At higher speeds in the other VTOL modes 1/4 and forward, which are not shown here, the control surfaces take over the majority of the control action while the four vertical rotors are switched off completely. Especially in roll and in VTOL mode 1/2, one sees that both control effectors contribute to the same maneuvers in a coordinated way.

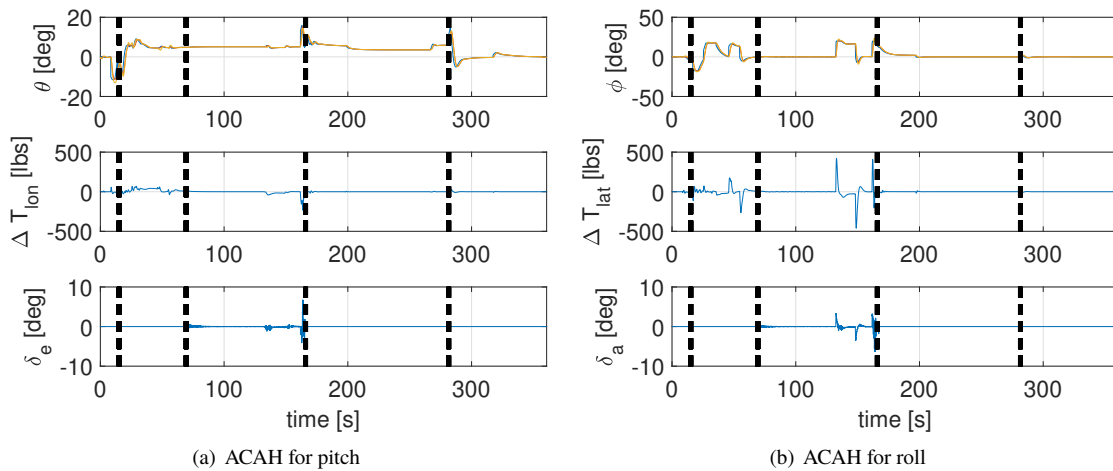


Fig. 14 ACAH modes for pitch and roll

2. Rate Command Direction Hold – Turn Coordination

For control in the directional axis, there are two different complementary modes, namely rate command direction hold (RCDH) for the heading ψ as well as turn coordination (TC) for the sideslip angle β . These are shown in Fig. 15(a) and 15(b) respectively. Each figure shows the aforementioned controlled variable on the top, with three time histories like in Fig. 14. These graphs illustrate which control mode is active per VTOL mode: RCDH works in hover mode and TC in all the others. Below the controlled variables, the corresponding inputs are given. Fig. 15(a) shows the directional thrust difference for the four vertical rotors $\Delta T_{\text{dir}} = (T_1 + T_4) - (T_2 + T_3)$ and Fig. 15(b) depicts the rudder deflection δ_r . The one control mode blends gradually towards the other during VTOL mode 3/4. It was found that the current blending works best for this design of vehicle. However, it is expected that other vehicle configurations, like e.g. quadrotor configurations without vertical tail, will require slightly different blending strategies.

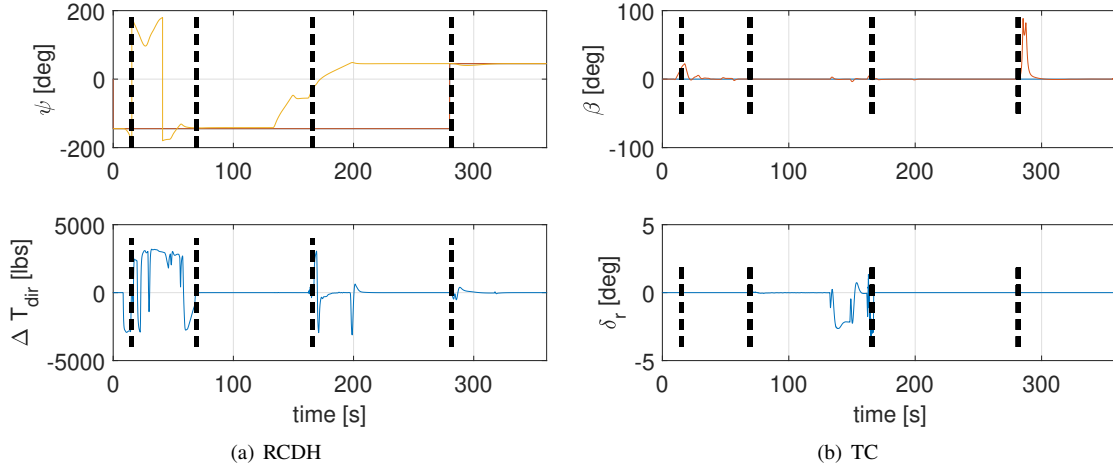


Fig. 15 RCDH and TC modes

3. Rate Command Height Hold and speed control with the main rotor nr 5

The Rate Command Height Hold mode (RCHH) controls the altitude. This is shown in Fig. 16(a). This mode is active anytime when the four vertical rotors T_{1-4} are active. Three time histories for altitude are shown here as well, namely the commanded value, together with the reference value (output of second order reference model), and the vehicle's response. These graphs show good tracking of the commanded values in all VTOL modes. Below the altitude as controlled variable, the corresponding inputs are given. Fig. 16(a) shows the total vertical thrust contribution for the four vertical rotors $\sum T_{\text{vert}}$, and it is clear that less vertical thrust is needed for higher airspeeds, because more lift is being generated by the airframe. Besides the RCHH mode, a speed control mode is needed whenever main rotor nr 5 is active. This is shown in Fig. 16(b). Below the calibrated airspeed as controlled variable, the corresponding thrust level of main rotor nr 5 is given. Both are correlated. Only at low maneuvering speeds in hover configuration, the main rotor nr 5 is switched off.

4. Translation Rate Command for approach and landing

The final control mode is the translational rate command mode (TRC), which is used at low speeds during takeoff, as well as for approach and landing. In this example, the most interesting flight phase is the approach and landing on the rooftop of the parking structure. Multiple scenarios were simulated and analyzed, and Fig. 17 focuses on two specific situations, namely vertical landing without and with wind. The challenge for both scenarios is that the vehicle must touch down within a circle of radius 50ft around the target landing spot. Fig. 17(a) shows the landing trajectory without wind. The vehicle transitions from slow forward flight with only a few knots at around 50 ft above the landing area, to a vertical landing towards the landing zone. The final touchdown point is only around 1.4ft from the reference point. Fig. 17(b) shows the similar trajectory with the aforementioned wind field. The vectors along the flightpath illustrate the relative wind speed and direction along the flight path. As previously mentioned, this wind field is non-uniform but steady, and also represents wind wakes around high rise buildings. This is particularly challenging,

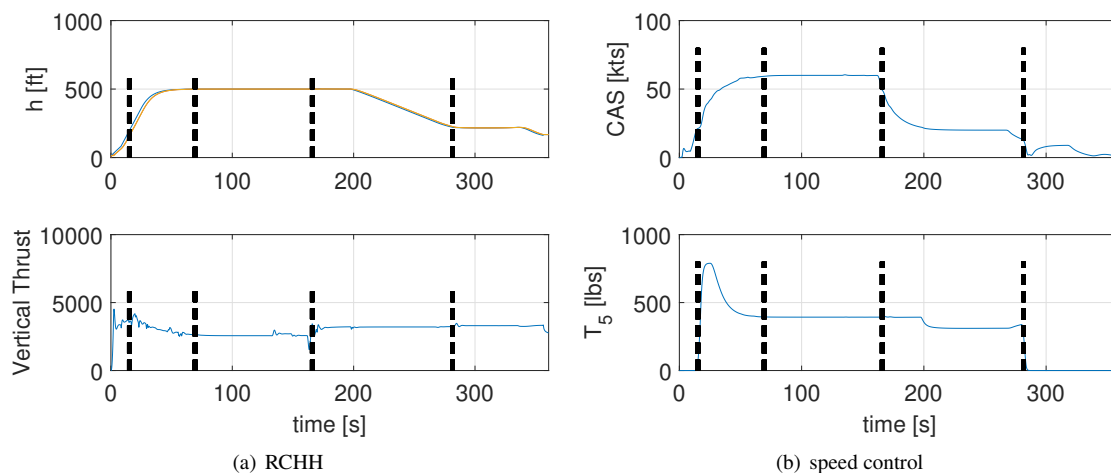


Fig. 16 RCHH mode and speed control

since the landing zone is surrounded by taller structures. The vehicle successfully compensates for drift caused by the wind while maneuvering towards the landing reference point at 50ft above the structure. However, while going down these last 50ft towards the landing zone, the wind direction and magnitude change again, as is shown by the changing vectors slightly above the touchdown point in Fig. 17(b). This results in an ultimate translational position correction of the vehicle. Due to the slow nature of these control actions, the deviation is not completely compensated for by the time of touchdown and the vehicle lands 12.5 ft from the landing reference point, which is still well within the 50 ft radius circle as required.

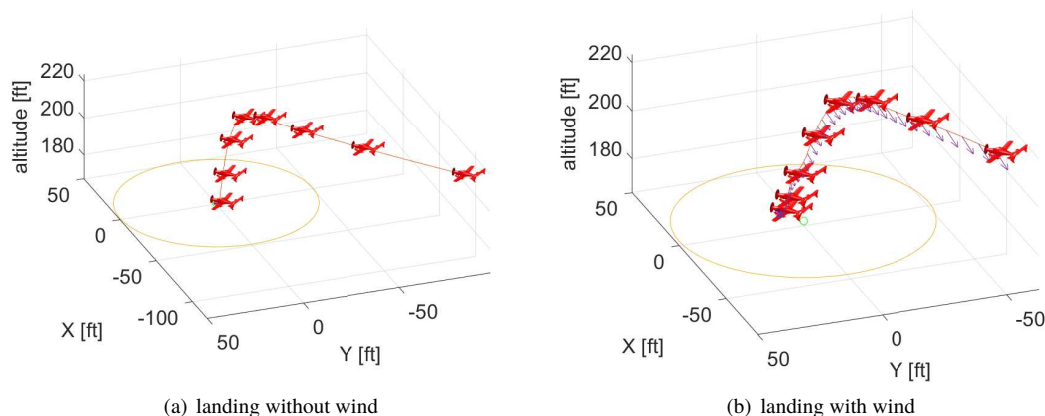


Fig. 17 TRC mode for approach and landing

B. Sample demo flight plan from San Francisco International Airport to downtown San Francisco

Fig. 18 shows the map and the 3D trajectory of a second sample demonstration mission, flown by means of a preprogrammed flightplan in the flight management system. The vehicle takes off vertically from San Francisco International Airport with heading 280 and flies via 3 waypoints towards the city of San Francisco after which it lands vertically on the rooftop of the parking structure at Mission and 5th. Compared to the previous scenario, this flight takes longer and includes a forward cruise flight phase. This permits a further analysis of the control modes and control allocation concept for the VTOL modes 1/4 and forward, which were not included in the previous example.

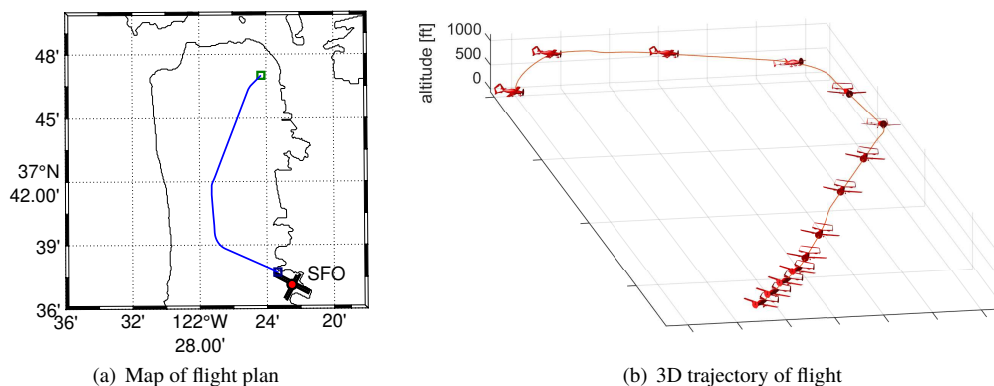


Fig. 18 Map and 3D trajectory of flight plan

Fig. 19 provides more detail on the flight phases of the longer demonstration flight. After the initial climb in hover mode, the vehicle pitches forward to speed up and activates the 5th main propeller to accelerate further to 120 kts while climbing to 1000 ft altitude. In the meantime the vehicle rapidly changes to VTOL modes 3/4, 1/2, 1/4 and finally forward. Halfway the circuit over the two enroute waypoints, the vehicle makes two consecutive right hand turns. Shortly after, the initial descent is started while the vehicle slows down to around 50 kts and transitions to VTOL modes 1/4, 1/2 and 3/4. Shortly after this speed capture, the vehicle starts to decelerate further towards 20 kts and descends towards 200ft. At this point, hover mode is activated and the 5th main prop is switched off. The vehicle maneuvers towards the landing area, and once it is lined up with the vertiport area, it descends vertically on the rooftop which is at 167 ft. The thicker blue lines in Fig. 19(a) as well as the vertical black dashed lines in Fig. 19(b) illustrate the moments when the VTOL mode changes. Fig. 19(a) shows the ‘transition corridor’ of the vehicle from hover towards full forwards cruise flight condition and vice versa. This flight was performed without wind.

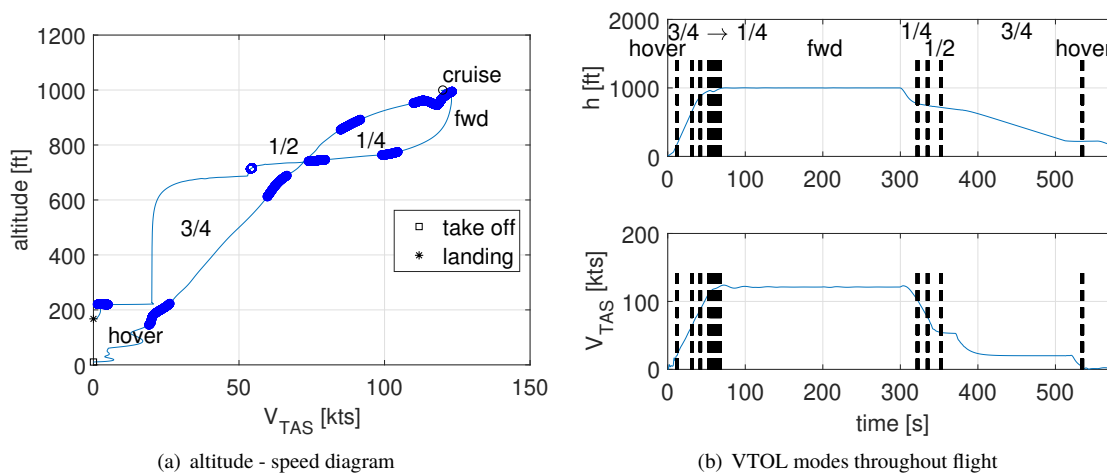


Fig. 19 altitude, speed and VTOL modes throughout the demo flight

Each VTOL mode, as illustrated in Fig. 19, corresponds with their respective control mode and propulsion configuration, as previously elaborated in Tab. 7.

The following sections elaborate on the different control modes and their respective control effectors discussed earlier. Compared to the previous scenario, these results focus on the forward cruise flight phase. The results are presented in a similar way as for the previous scenario.

1. Attitude and Rate Command Attitude Hold

The attitude and rate command attitude hold (ACAH/RCAH) modes works for two axes, namely longitudinally for pitch, as shown in Fig. 20(a) and laterally for roll, illustrated in Fig. 20(b). RCAH works in forward flight only, with ACAH in all other modes. These graphs show good tracking of the commanded values in all VTOL modes. Fig. 20(a) shows the longitudinal thrust difference for the four vertical rotors $\Delta T_{lon} = (T_1 + T_2) - (T_3 + T_4)$ and the elevator deflection δ_e , in Fig. 20(b) these are the lateral thrust difference for the four vertical rotors $\Delta T_{lat} = (T_1 + T_3) - (T_2 + T_4)$ and the aileron deflection δ_a . Analyzing these figures shows that only the thrust differences control the vehicle in VTOL modes hover and 3/4, since the control surfaces are not yet effective in these low speed flight conditions. The control surfaces become active in VTOL mode 1/2 and support the four rotors which are becoming less effective at higher speeds. At higher speeds in the other VTOL modes 1/4 and forward, the control surfaces take over the majority of the control action while the four vertical rotors are switched off completely in the forward flight mode. One observes also that there is more control action in roll than in pitch, due to the larger angles which are established during the maneuvers. Especially in roll and in VTOL mode forward, one sees that only the control surfaces are active. This is less visible in pitch.

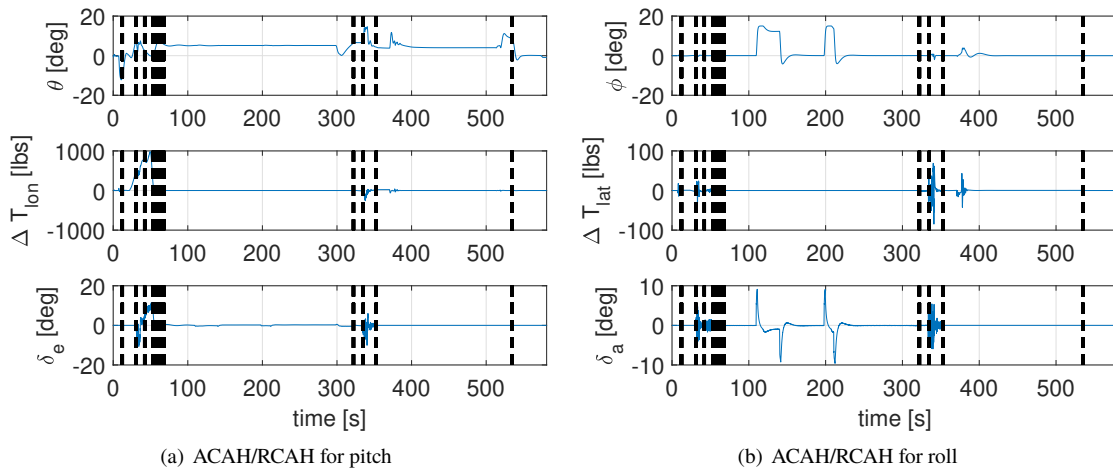


Fig. 20 ACAH/RCAH modes for pitch and roll

2. Rate Command Direction Hold – Turn Coordination

For control in the directional axis, there are two different complementary modes, as explained before. These are rate command direction hold (RCDH) for the heading ψ as well as turn coordination (TC) for the sideslip angle β , and they are shown in Fig. 21(a) and 21(b) respectively. These graphs illustrate which control mode is active per VTOL mode: RCDH works in hover mode and in 3/4 at low enough speeds and TC in all the others. Fig. 21(a) shows the directional thrust difference for the four vertical rotors $\Delta T_{dir} = (T_1 + T_4) - (T_2 + T_3)$ and Fig. 21(b) depicts the rudder deflection δ_r . The one control mode blends gradually towards the other during VTOL mode 3/4. The complementary nature of both modes is nicely illustrated in Fig. 21. In forward cruise flight, the rudder controls the sideslip angle in TC mode as shown in Fig. 21(b). For the low speed turn during the approach, the directional thrust difference is used to control the heading change in RCDH mode as shown in Fig. 21(a).

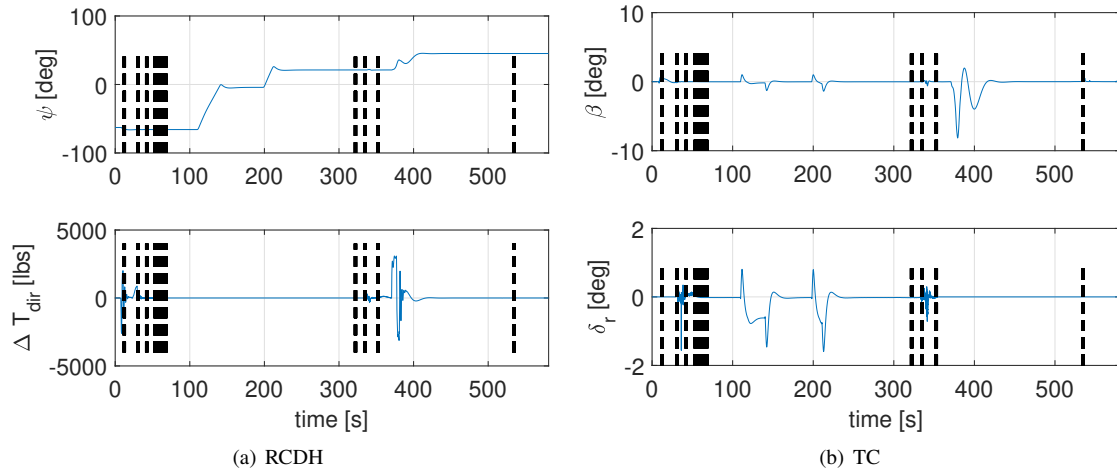


Fig. 21 RCDH and TC modes

3. Rate Command Height Hold and speed control with the main rotor nr 5

The Rate Command Height Hold mode (RCHH) controls the altitude. This mode is active anytime when the four vertical rotors T_{1-4} are active. Fig. 22(a) shows the total vertical thrust contribution for the four vertical rotors $\sum T_{vert}$, and it is clear that less vertical thrust is needed for higher airspeeds, because more lift is being generated by the airframe. In forward flight, the total vertical thrust reduces to zero since this is wing-borne flight. However, it is expected that other vehicle configurations, like e.g. quadrotor configurations without wings, will require vertical thrust during forward flight as well.

Besides the RCHH mode, a speed control mode is needed whenever main rotor nr 5 is active. This is shown in Fig. 22(b). Below the calibrated airspeed as controlled variable, the corresponding thrust level of main rotor nr 5 is given. Both are correlated. Only during the initial steep descent and at low maneuvering speeds in hover configuration, the main rotor nr 5 is switched off.

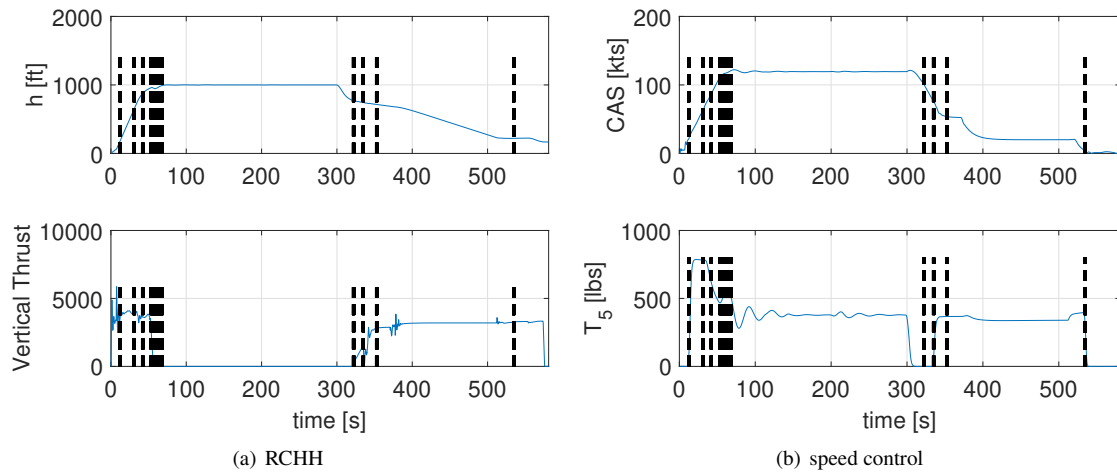


Fig. 22 RCHH mode and speed control

4. Translation Rate Command for approach and landing

The final control mode is the translational rate command mode (TRC). Fig. 23 shows the landing trajectory. The vehicle transitions from slow forward flight with only a few knots at around 50 ft above the landing area, to a vertical landing towards the landing zone. The final touchdown point is only around 4ft from the reference point, well within a circle of radius 50ft.

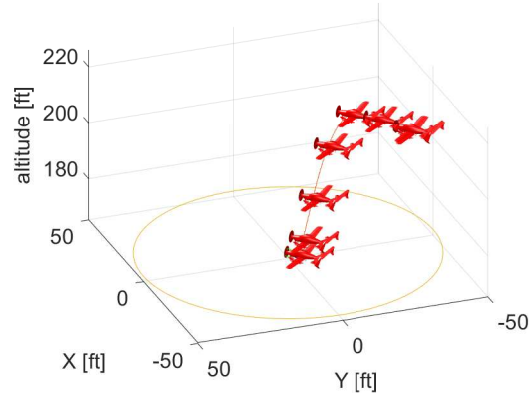


Fig. 23 TRC mode for approach and landing without wind

C. Translational Rate Command compliance with ADS-33 Requirements

ADS-33, [42], mentions the following requirements for translational rate control:

- 1) TRC response to a step input must demonstrate a qualitative first order appearance, with a rise time T between 2.5 and 5s.
- 2) There should be no objectionable overshoots in pitch and roll attitudes.
- 3) Zero cockpit deflection corresponds to zero translational rate.
- 4) There should be no noticeable overshoots in the responses of the translational rates to the control inputs.

Fig. 24(a) shows that these criteria are met. The rise times for forwards and lateral translational rates are both around 3.5s, which is between the required values of 2.5 and 5s. Moreover, there is significant margin to both boundaries. Testing has shown that the reference acceleration feedforward term in Eq. 67 – 68 is crucial for fulfilling the rise time requirement.

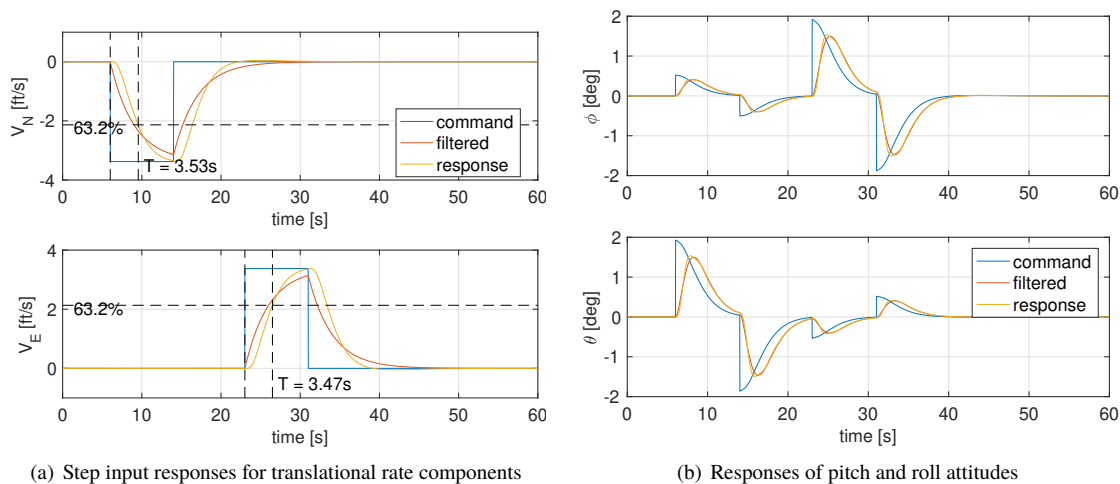


Fig. 24 Performance of Translational Rate Control

VI. Conclusions and recommendations

In this research, nonlinear dynamic inversion (NDI) as well as incremental nonlinear dynamic inversion (INDI) was applied for integrated full envelope flight control of a lift plus cruise eVTOL vehicle, using a unified framework. Both approaches have the following advantages: (1.) Perfect decoupling of the steering channels, which results in a significantly simplified steering task. (2.) The control laws are split in an airframe dependent part and an airframe independent part. In this way, gain scheduling is not needed. (3.) The total control structure involves reference models for command shaping. This is a good method for complying with flying and handling qualities and for incorporating future planned functionalities in the control setup. (4) Internal flight control states have a physical meaning and are interpretable. INDI has the additional advantage that it is less dependent on aerodynamic modeling parameters. This is particularly useful for eVTOL UAM vehicles, since it is expected that the available aerodynamic modeling information of these vehicles will be limited. Analysis of the translational rate command mode for landing and precision maneuvering with respect to the ground indicated that its closed loop performance satisfies all relevant ADS-33 handling qualities requirements. Prioritized control allocation by means of weighted least squares was successfully implemented and evaluated in a series of evaluations in representative scenarios.

This flight control design results in an overall closed loop system with satisfactory performance throughout the full flight envelope that can serve as a baseline for further evaluations and developments. Pseudo control hedging and safe flight envelope protection limits must be added to the reference models in this control setup and fault tolerance to certain failures, such as a rotor failure, must be analyzed. Fault tolerance will be a crucial aspect, as well as easy handling and ‘carefree flying’ capability, which will include some kind of envelope protection for upset prevention.

Acknowledgments

The authors would like to thank Joe Totah for his support and expert advice in developing the propulsion simulation model as described in Sec. II.II.B. The CFD windfield was provided by the NASA Ames Systems Analysis Office.

References

- [1] Swartz, K. I., “Charging Forward - New eVTOL Concepts Advance,” *Vertiflite*, 2017.
- [2] Johnson, W., Silva, C., and Solis, R., “Concept Vehicles for VTOL Air Taxi Operations,” *AHS Technical Conference on Aeromechanics Design for Transformative Vertical Flight*, 2018.
- [3] Silva, C., Johnson, W. R., Solis, E., Patterson, M. D., and Antcliff, K. R., “VTOL Urban Air Mobility Concept Vehicles for Technology Development,” *2018 Aviation Technology, Integration, and Operations Conference*, American Institute of Aeronautics and Astronautics, 2018. doi:10.2514/6.2018-3847.
- [4] Antcliff, K., and Kohlman, L. W., “Technology Targets and Research Areas for Urban Air Mobility Vehicles,” *AIAA Scitech 2019 Forum*, American Institute of Aeronautics and Astronautics, 2019. doi:10.2514/6.2019-0528.
- [5] Lombaerts, T., Kaneshige, J., Schuet, S., Hardy, G., Aponso, B. L., and Shish, K. H., “Nonlinear Dynamic Inversion Based Attitude Control for a hovering quad tiltrotor eVTOL vehicle,” *AIAA Scitech 2019 Forum*, American Institute of Aeronautics and Astronautics, 2019. doi:10.2514/6.2019-0134.
- [6] Raab, S. A., Zhang, J., Bhardwaj, P., and Holzapfel, F., “Proposal of a Unified Control Strategy for Vertical Take-off and Landing Transition Aircraft Configurations,” *2018 Applied Aerodynamics Conference*, American Institute of Aeronautics and Astronautics, 2018. doi:10.2514/6.2018-3478.
- [7] Achtelik, M., Bierling, T., Wang, J., Höcht, L., and Holzapfel, F., “Adaptive Control of a Quadcopter in the Presence of large/complete Parameter Uncertainties,” *AIAA Infotech@Aerospace*, American Institute of Aeronautics and Astronautics AIAA, 2011. doi:10.2514/6.2011-1485.
- [8] Yanguo, S., and Huanjin, W., “Design of Flight Control System for a Small Unmanned Tilt Rotor Aircraft,” *Chinese Journal of Aeronautics*, Vol. 22, No. 3, 2009, pp. 250–256. doi:10.1016/S1000-9361(08)60095-3.
- [9] Francesco, G. D., and Mattei, M., “Modeling and Incremental Nonlinear Dynamic Inversion Control of a Novel Unmanned Tiltrotor,” *Journal of Aircraft*, Vol. 53, No. 1, 2016, pp. 73–86. doi:10.2514/1.C033183.
- [10] Sieberling, S., Chu, Q. P., and Mulder, J. A., “Robust Flight Control Using Incremental Nonlinear Dynamic Inversion and Angular Acceleration Prediction,” *Journal of Guidance, Control, and Dynamics*, Vol. 33, No. 6, 2010, pp. 1732–1742. doi:10.2514/1.49978.

- [11] Smeur, E., de Croon, C., and Chu, Q., "Cascaded Incremental Nonlinear Dynamic Inversion Control for MAV Disturbance Rejection," *Control Engineering Practice*, Vol. 73, 2018, pp. 79–90. doi:10.1016/j.conengprac.2018.01.003.
- [12] Wang, X., van Kampen, E.-J., Chu, Q., and Lu, P., "Stability Analysis for Incremental Nonlinear Dynamic Inversion Control," *AIAA SciTech Forum*, American Institute of Aeronautics and Astronautics, 2018. doi:10.2514/6.2018-1115.
- [13] Matamoros, I., and de Visser, C. C., "Incremental Nonlinear Control Allocation for a Tailless Aircraft with Innovative Control Effectors," *2018 AIAA Guidance, Navigation, and Control Conference*, American Institute of Aeronautics and Astronautics, 2018. doi:10.2514/6.2018-1116.
- [14] Roskam, J., *Airplane Flight Dynamics and Automatic Flight Controls*, DARcorporation, 1995, Chap. Stability and Control Derivatives for a small general aviation airplane such as the Cessna 182, pp. 480 – 486.
- [15] Hoerner, S. F., and Borst, H. V., *Fluid-Dynamic Lift, Practical Information on Aerodynamic and Hydrodynamic Lift*, Mrs. Liselotte A. Hoerner, 1985.
- [16] Hoerner, S. F., *Fluid-Dynamic Drag, Practical Information on Aerodynamic Drag and Hydrodynamic Resistance*, Sighard F. Hoerner, 1965.
- [17] Totah, J. J., "Mathematical Model of a Tiltwing Aircraft," *47th Annual Forum of the Amecian Helicopter Society*, 1991.
- [18] Chu, Q., *Lecture Notes AE4-394, Modern Flight Test Technologies and System Identification*, Delft University of Technology, Faculty of Aerospace Engineering, 2007.
- [19] Slotine, J.-J. E., and Li, W., *Applied Nonlinear Control*, Prentice Hall, 1991.
- [20] Lombaerts, T., and Looye, G., "Design and flight testing of manual nonlinear flight control laws," *AIAA Guidance, Navigation and Control Conference*, 2011. doi:10.2514/6.2011-6469.
- [21] Lombaerts, T., and Looye, G., "Design and flight testing of nonlinear autoflight control laws," *AIAA Guidance, Navigation, and Control Conference*, American Institute of Aeronautics and Astronautics, 2012. doi:10.2514/6.2012-4982.
- [22] Grondman, F., Looye, G., Kuchar, R. O., Chu, Q. P., and Kampen, E.-J. V., "Design and Flight Testing of Incremental Nonlinear Dynamic Inversion-based Control Laws for a Passenger Aircraft," *2018 AIAA Guidance, Navigation, and Control Conference*, American Institute of Aeronautics and Astronautics, 2018. doi:10.2514/6.2018-0385.
- [23] van Ekeren, W., Looye, G., Kuchar, R. O., Chu, Q. P., and Kampen, E.-J. V., "Design, Implementation and Flight-Tests of Incremental Nonlinear Flight Control Methods," *2018 AIAA Guidance, Navigation, and Control Conference*, American Institute of Aeronautics and Astronautics, 2018. doi:10.2514/6.2018-0384.
- [24] Pollack, T., Looye, G., and van der Linden F.L.J., "Design and flight testing of flight control laws integrating incremental nonlinear dynamic inversion and servo current control," *AIAA SciTech Conference*, American Institute of Aeronautics and Astronautics, 2019. doi:10.2514/6.2019-0130.
- [25] Keijzer, T., Looye, G., Chu, Q., and van Kampen, E.-J., "Design and Flight Testing of Incremental Backstepping based Control Laws with Angular Accelerometer Feedback," *AIAA SciTech Conference*, 2019. doi:10.2514/6.2019-0129.
- [26] Zhang, Y., and Jiang, J., "Bibliographical review on reconfigurable fault-tolerant control systems," *Annual Reviews in Control*, Vol. 36, No. 5, 2008, pp. 257–268. doi:https://doi.org/10.1016/j.arcontrol.2008.03.008.
- [27] Smeur, E., Hoppener, D., and De Wagter, C., "Prioritized Control Allocation for Quadrotors Subject to Saturation," *International Micro Air Vehicle Conference and Flight Competition (IMAV)*, 2017, pp. 37–43. URL http://www.imavs.org/papers/2017/51_imav2017_proceedings.pdf.
- [28] Johansen, T., Fossen, T. T. A. J., and Fossen, T. I., "Control Allocation – A Survey," *Automatica*, Vol. 49, 2013, pp. 1087–1103. doi:10.1016/j.automatica.2013.01.035.
- [29] Harkegard, O., "Efficient Active Set Algorithms for Solving Constrained Least Squares Problems in Aircraft Control Allocation," *41th IEEE Conference on Decision and Control*, 2002. doi:10.1109/CDC.2002.1184694.
- [30] Johnson, E. N., and Calise, A. J., "pseudo-control hedging: a new method for adaptive control," *Advances in Navigation Guidance and Control Technology Workshop*, 2000. URL soliton.ae.gatech.edu/people/ejohnson/ngct-paper-johnson.pdf.

- [31] Holzapfel, F., "Dynamic Inversion Based Control Concept with Application to an Unmanned Aerial Vehicle," *AIAA Guidance, Navigation, and Control Conference and Exhibit*, 2004. doi:10.2514/6.2004-4907.
- [32] Holzapfel, F., "Nichtlineare adaptive Regelung eines unbemannten Fluggerätes," Ph.D. thesis, Lehrstuhl für Flugmechanik und Flugregelung, Technische Universität München, 2004. URL <https://mediatum.ub.tum.de/doc/601905/601905.pdf>.
- [33] Lombaerts, T., Looye, G., Chu, Q., and Mulder, J., "Pseudo Control Hedging and its Application for Safe Flight Envelope Protection," *AIAA Guidance, Navigation and Control Conference*, 2010. doi:10.2514/6.2010-8280.
- [34] Lombaerts, T., Schuet, S., Wheeler, K., Acosta, D., and Kaneshige, J., "Safe Maneuvering Envelope Estimation based on a Physical Approach," *AIAA Guidance, Navigation and Control (GNC) Conference*, 2013. doi:10.2514/6.2013-4618.
- [35] Schuet, S., Lombaerts, T., Acosta, D., Wheeler, K., and Kaneshige, J., "Autonomous Flight Envelope Estimation for Loss-of-Control Prevention," *Journal of Guidance, Control and Dynamics*, , No. AIAA 2014-0268, 2016. doi:10.2514/1.g001729.
- [36] Lombaerts, T., Looye, G., Ellerbroek, J., and Rodriguez y Martin, M., "Design and Piloted Simulator Evaluation of Adaptive Safe Flight Envelope Protection Algorithm," *Journal of Guidance, Control and Dynamics*, 2017. doi:10.2514/1.G002525.
- [37] Lombaerts, T., Looye, G., Seefried, A., Neves, M., and Bellmann, T., "Proof of concept simulator demonstration of a physics based self-preserving flight envelope protection algorithm," *Engineering Applications of Artificial Intelligence*, Vol. 67, 2018, pp. 368–380. doi:10.1016/j.engappai.2017.08.014.
- [38] Simplicio, P., Pavel, M., van Kampen, E., and Chu, Q., "An acceleration measurements-based approach for helicopter nonlinear flight control using Incremental Nonlinear Dynamic Inversion," *Control Engineering Practice*, Vol. 21, 2013, pp. 1065–1077. doi:10.1016/j.conengprac.2013.03.0009.
- [39] Johnson, E. N., "Limited Authority Adaptive Flight Control," phdthesis, Georgia Institute of Technology, Nov. 2000. URL <https://pdfs.semanticscholar.org/0f6e/2cef3b5a5c9043a7ec6c4319ecebba868af1.pdf>.
- [40] Lock, A., "San Francisco City 3D Model," Online Library Archive, Nov. 2008. URL <https://www.3dcadbrowser.com/3d-model/san-francisco-city>, retrieved December 2019.
- [41] "STAR-CCM+," 2019. URL <https://www.plm.automation.siemens.com/global/en/products/simcenter/STAR-CCM.html>.
- [42] "Aeronautical Design Standard, Performance Specification, Handling Qualities Requirements for Military Rotorcraft," Tech. Rep. ADS-33E-PRF, United States Army Aviation and Missile Command Aviation Engineering Directorate, Mar. 2000. URL <https://www.amrdec.army.mil/amrdec/rdmr-se/tdmd/Documents/ads33front.pdf>.